Algorithms for Recognition of Low Quality Iris Images

by

Li Peng Xie

Thesis submitted to the
Faculty of Graduate and Postdoctoral Studies
In partial fulfillment of the requirements
For the M.A.Sc. degree in
Electrical and Computer Engineering

School of Information Technology and Engineering
Faculty of Engineering
University of Ottawa

Abstract

A biometric system is designed to accurately identify people based on human physiological features such as face, iris, fingerprint and voice recognition. Iris recognition is considered to have the highest identification accuracy and commercial iris recognition systems have been deployed in many applications, like passports and border control.

One of the key performance limitations in iris recognition is the low image quality, including rotated iris images, partial eyelash and eyelid occlusions.

We developed an algorithm to accurately detect the eyelash occlusion and eliminate these eyelash occluded regions from the recognition. The resulting detection error tradeoff curve showed an improved error rate in most of the false match (FMR) rate range. We also examined two methods of rotational invariant feature extraction: one based on the covariance features and one based on the Fourier transform magnitudes. In addition, we evaluated the errors in the localizations of circles. The system performance after correction was re-evaluated, and a marginal improvement was observed, in terms of the rank-1 identification rate, the DET curve, and the cumulative match curve. Moreover, we tested a progressive segmentation scheme. It gradually increased the area of the iris region that was segmented for the inter-class and intra-class comparisons. It showed that in a particular range of an iris image area, the system performance improves rapidly.

Overall, this thesis suggests that it is possible to improve the iris recognition with low quality iris images. It also provides several research directions for future work.

Acknowledgements

Many people have accompanied and helped me through my two years of study, and without them it would have been impossible for me to arrive at today.

I must thank Dr. Andy Adler, my supervisor, for his encouragement and guidance. His research experience gave me insights into my thesis and understanding of various aspects of this research subject. The time and effort he spent with me on my project, reviewing my thesis was invaluable and an ever-lasting influence. The traveling, mountain biking and Christmas get-together that we had enjoyed over the years are unforgettable.

I really appreciate the help and motivation received from my friend and colleague, Richard Youmaran. His knowledge and skills with image processing techniques have given lots of help with my project progress. I also feel lucky for knowing and working with many other interesting people during the past two years, which comprised an episode of fun and joy in my spare time. I enjoyed fishing with Tao Dai, football with Camille Gomez, card games with Tanya Petrenko, road trips with Yednek Asfaw, mountain biking with Ran Klein, and ice-skating with David Bryan.

And my parents, my long-time and steadfast supporters and advisors, backing me up both emotionally and financially, for which I will never have enough to pay back.

Contents

List of Figures

Nomenclature

NC Normalized Correlation

FFT Fast Fourier Transform

RI Rotational Invariance

LoG Laplacian of Gaussian

DET Detection Error Trade-off

FDA Fisher Discriminant Analysis

LDA Linear Discriminant Analysis

CMC Cumulative Match Curve

Gen-Imp Genuine-Imposter Distribution

DCAC Discrete Circular Active Contour

FAR False Accept Rate

FRR False Reject Rate

FMR False Match Rate

FNMR False Non Match Rate

EER Equal Error Rate

HD Hamming Distance

IR Infrared

NIR Near Infrared

PCA Principal Component Analysis

ROC Receiver Operating Characteristic

SVD Singular Value Decomposition

WED WEighted Eulidean Distance

Chapter 1

Introduction

1.1 Iris Recognition

In recent years, the accurate surveillance and access control have been given a lot of attention because of the potential security threats. Biometric technologies are able to achieve the personal identification and verification based on the physiological and behavioral characteristics of the subject. Currently, there are various biometric technologies, such as fingerprint recognition, face recognition, iris recognition and voice recognition [1]. Some of these technologies are intrusive, like fingerprint recognition, which requires skin contact between the subject and the imaging facility [2]. Some other technologies have relatively low recognition rates, like face recognition [3] and speaker recognition [4]. For the above reasons, iris recognition shows the advantages of non-intrusiveness and higher accuracy. It is non-intrusive, since it only requires the subject to look into the camera for iris image acquisition. It also has a very high identification rate, because of the unique texture patterns and abundant information contained in iris images.

With the current development of iris recognition technology, there are still problems to be solved to improve the system performance. Recognition based on low-quality iris images is a particularly interesting area. Some low-quality iris images are partially occluded by the eyelid and eyelash regions. Other iris images could be rotated before recognition and processing, and therefore they require rotation compensations before the cross-comparisons between iris feature templates.

Here we give a brief introduction of the iris recognition system and its components as well as a major literature review. There are many ways to classify the components of a biometric system. One way is to divide the system into five blocks: data collection,

transmission, signal processing, storage and decision [5]. In this thesis, we break down an iris recognition system in a similar way in terms of image processing procedures: image acquisition, iris localization and segmentation, registration, feature extraction, and pattern matching.

1.2 Iris Texture and Image Acquisition

1.2.1 Iris structure and unique texture pattern

Iris structure

The iris anatomy has a multi-layered structure. The most posterior layer is comprised of epithelial cells containing iris pigments. The anterior layer is comprised of two sets of muscles, the sphincter muscle and the dilator muscle. The former one contracts the pupil and the latter one opens it. Further into the anterior side is the stromal layer, a layer of collagenous tissues. This layer generates the most part of an iris image. The most anterior layer is the border layer [6].
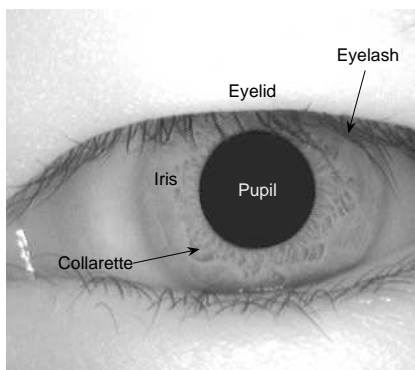
Figure 1.1: Iris structure.

Iris textures and colors

The iris texture features are formed by various components within the iris. These components include crypts, furrows, arching, collarette and rings of various shapes. Also, these components are filled with color pigments, such as green, red and blue. The natural iris

colors observed by humans are generated mostly from a combination of melanin pigments [7], mostly in the anterior layer and stromal layer. Visible light goes through the iris, and the absorption and reflection of light depend on the wavelength. The variation in the pigment density determines the amount and combination of the reflected light spectrum, which further determines the color of the iris.

In iris recognition, near infrared (NIR) cameras are usually used instead of visible light. The NIR camera applies a wavelength spectrum from 700 nm to 900 nm (Iridian Technology 2005), which emphasizes the texture pattern accurately, especially when it comes to darker regions. Another reason for the use of NIR lighting is that it is a more comfortable and mild light source, and therefore it does not irritate the subject as would the regular light source. In this project, the database applied was acquired with NIR light cameras.

The unique and abundant texture patterns in the iris images are "determined epigenetically by random events in the morphogenesis process", as stated by John Daugman [8]. Moreover, the cross-comparisons are performed between genetically identical images, taken from the left and right eyes of the same persons. It shows that the statistical distributions are the same between genetically identical subjects and genetically unrelated subjects. Furthermore from 2001 to 2005, a project was conducted by the University of Cambridge and the United Arab Emirates interior ministry. In this project, 632500 iris images were acquired in the Middle East and over 200 billion cross-comparisons were generated between different eyes. With the Daugman algorithm and an appropriate threshold setting, it achieved a false match rate (FMR) of less than 1 in 200 billion [9].

However, it seems too idealistic to claim an FMR of 1 in 200 billion. Recently, three third-party evaluations of iris recognition algorithms were performed by independent institutions, based on individually collected iris image databases. In the comparison results, a similar range of a false non-match rate (FNMR) from 0.01 to 0.03 is observed, when examined with a common FMR of 0.001 [10, 11, 12].

Stability with age

One characteristic of iris images, when they are used as biometric information templates, is the stability with age as compared to face recognition, in which the facial images and features could vary dramatically over time. Even facial expressions could be largely different within one day. Ophthalmologists and anatomists have observed that the iris patterns change to a very small extent, keeping most of its original features across the lifetime [13]. From the explanations of development biology, a healthy iris keeps most of

its forms and patterns after the adolescence period [6, 14].

1.2.2 Imaging Systems

Currently, two well-known iris imaging algorithms are developed individually by the John Daugman group and the Richard Wildes group. As far as commercially distributed systems, there are several companies engaged in the design, research and manufacture of iris recognition systems, including LG, Oki, Iridian and Panasonic.

Both the Daugman and the Wildes algorithms use monochrome gray-scale images, which provide enough information to achieve satisfactory identification rates. The main difference between these two imaging systems is the lighting source implementation. The Daugman system uses a light source from the side, while the Wildes system applies a diffuser to illuminate the entire eye region uniformly.

The Daugman system

In the Daugman system, the light source is placed to the side of the eye, as shown in Fig 1.2. The light is reflected and captured by a camera after going through a beam splitter. The captured iris image typically has a diameter of 100 to 200 pixels, which gives sufficient information for iris recognition.

The Wildes system

The imaging system developed by the Wildes team applies a series of light sources, illuminating the iris region through a diffuser and a circular polarizer, as shown in Fig 1.3. The captured iris image has a diameter of around 256 pixels. The benefit of this schematic is that the strong specular reflections generated from a single light source are reduced because of the more evenly distributed light illumination [15].

As far as the type of light used, both of these former systems applied a visible light spectrum initially. Later on, the use of a near infrared light source was proposed for the advantage of the more detailed and complex features from the stromal regions, because the visible light sources revealed only human visible ligament meshwork.

Daugman Imaging System for Iris Recognition
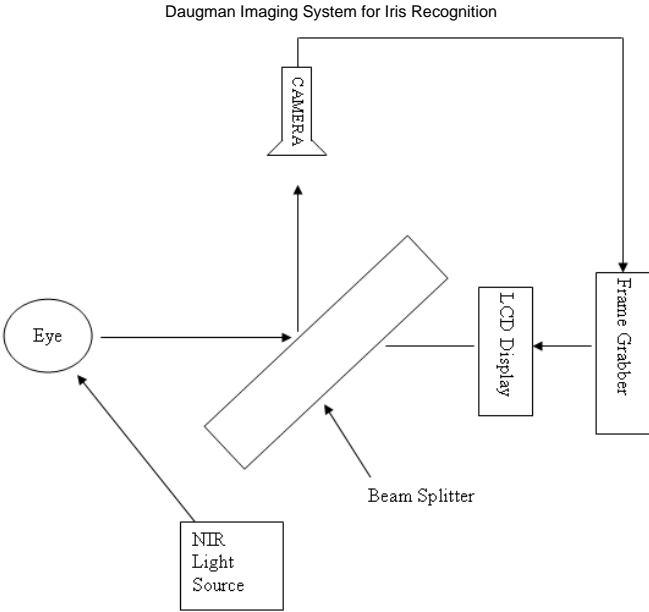
Figure 1.2: The Daugman iris imaging system diagram [13].
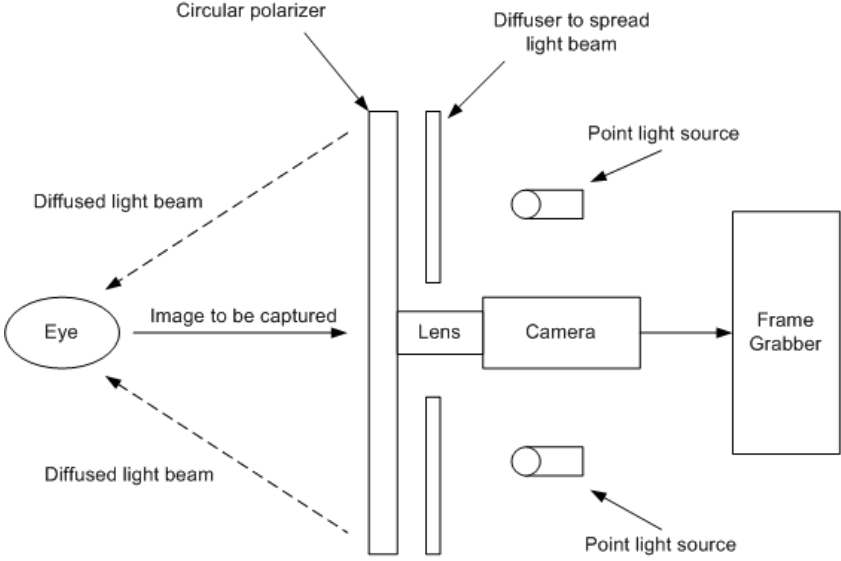
Figure 1.3: The Wildes iris imaging system diagram [13].

1.3   Iris Localization and Segmentation

Iris localization and segmentation accomplish the job of determining the specific iris region from an eye image, mainly the iris boundary, the pupil boundary, the upper eyelid and lower eyelids. The artifacts could exist commonly within the iris images, such as the eyelash occlusion, the eyelid occlusion and the image noise. A successful removal of these artifacts generates the clean iris region for the subsequent recognition. Moreover, various methods have been proposed to identify and eliminate the artifacts in iris images, particularly the eyelash occlusion and specular reflections.

1.3.1   Integro-differential operator

John Daugman proposed to use the integro-differential operator to locate the pupil and iris circles as well as the upper and lower eyelid boundaries [7].

$$max_{(r,x_0,y_0)} \mid G_\sigma(r) * \frac{\partial}{\partial r} \oint_{r,x_0,y_0} \frac{I(x,y)}{2\pi r} ds \mid \tag{1.1}$$

$$G_\sigma(r) = \frac{1}{\sqrt{2\pi}\sigma} e^{-\frac{(r-r_0)^2}{2\sigma^2}} \tag{1.2}$$

in which $I(x,y)$ is the entire iris image to search for the iris region, (r, x_0, y_0) represents a circle to be searched with a radius r and center coordinates (x_0, y_0), and $G_\sigma(r)$ is a radial Gaussian smoothing function with the center r and the standard deviation σ.

In general, this function searches through the whole image (x, y) for integrations along different circular contours with center coordinates (x_0, y_0) and an increasing radius r. The maximum contour integral derivative corresponds to the most likely circle tracing the iris. As is used in the segmentation of iris images, the circular boundaries for the pupil and iris regions are localized by searching through the entire iris image for the maximum integration along various circular contours.

Moreover, in the Daugman system, the upper and lower eyelids are also approximated with two open curves that are part of two separate circles. The same method is also used to find the boundaries of these two circles that go through the upper and lower eyelid. Thus, the iris region used for feature extraction and pattern recognition is the area surrounded by the upper eyelid, the lower eyelid, the circular pupil boundary and the circular iris boundary.

1.3.2 Circular Hough Transform

Gradient-based edge detection, followed by the circular Hough transform is a standard machine vision technique to find circular contours in images. Many iris recognition systems apply this technique to find the iris boundary contours, including the Wildes system [13].

First, the entire image $I(x, y)$ is smoothed with a Gaussian filter $G(x, y)$ as in Equation 1.3. The Gaussian filter is defined as in Equation 1.4, centered at (x_0, y_0) with a standard deviation of σ.

$$F(x, y) = G(x, y) * I(x, y) \tag{1.3}$$

$$G(x, y) = \frac{1}{2\pi\sigma^2} e^{-\frac{(x-x_0)^2 + (y-y_0)^2}{2\sigma^2}} \tag{1.4}$$

The intensity gradient image map $M(x, y)$ is generated from the smoothed image $F(x, y)$, as shown in Equation 1.5. The gradient operation is defined in Equation 1.6. Then, the binary edge map is generated by setting a threshold on the intensity gradient image $M(x, y)$.

$$M(x, y) = |\nabla F(x, y)| \tag{1.5}$$

$$\nabla \equiv (\partial/\partial x, \partial/\partial y) \tag{1.6}$$

From the binary image map, the Hough transform is performed to locate a circle with the largest number of edge points and its circular parameter set(x_0, y_0, r) could be modeled as:

$$(x_i - x_0)^2 + (y_i - y_0)^2 = r^2 \tag{1.7}$$

in which (x_0, y_0, r) represents a circle to be searched with the radius r, and the center coordinates (x_0, y_0), and (x_i, y_i) represents one of the possible edge points.

The Hough transform is performed through the entire collection of the edge points. Whenever Equation 1.7 is satisfied, it means that the circular contour (x_0, y_0, r) goes through this point, and one vote is added to the histogram of this contour. In the end, the contour with the highest histogram or votes represents the most likely circle in the edge map.

1.3.3 Discrete Circular Active Contour Model

Nicola Ritter *et al.* [16] applied the circular active contour model to locate the pupil and iris boundaries. First, the variance image is generated from the original image, and this variance image is used to localize the pupil region. Then, an active contour with a starting point in the center of the pupil is initiated and moved within the iris image under the influence of so called "the internal and external forces". Along the active contour, the vertex v moves from time t to time $t + 1$ according to:

$$v_i(t + 1) = v_i(t) + F_i(t) + G_i(t) \qquad (1.8)$$

in which v_i represents the location of the vertex, from position at time t to $t + 1$, and F_i represents the internal force and G_i represents the external force.

The internal force relies on certain characteristics like the continuity, and other prior knowledge about the iris boundary (like its circular shape). The external force is based on the gray-scale intensity values immediately inside and outside the vertex, which confines the contour within the iris region. The result of this iterative contour searching is the equilibrium with minimum energy or minimum mean variance of the annulus, which gives the final iris segmentation for later processing.

1.3.4 Noise and Artifacts in Iris Images

Noise and artifacts exist in iris images, and they have a negative impact on the system performance. Such artifacts include the eyelash occlusion, the eyelid occlusion and the specular reflections.

Fig 1.4 shows an example of an iris image contaminated with both eyelash occlusion and eyelid occlusion. It is clearly illustrated that part of the image is covered by the top and bottom eyelids, and they do not represent true iris image information. Furthermore, the eyelashes that spread across the image also modified the regions intended for iris recognition use. Therefore, they should be detected and eliminated from the subsequent recognition process.

Specular reflections are mirror-like reflections, such as the light reflected on a tranquil water surface. Similarly in the iris image acquisition procedure, the specular reflections occur in such a way that the light source gets reflected and imaged by the camera. The strong reflection intensity in the image results in high pixel values which deviate absolutely from the original iris patterns. Fig 1.5 shows an example of iris image with
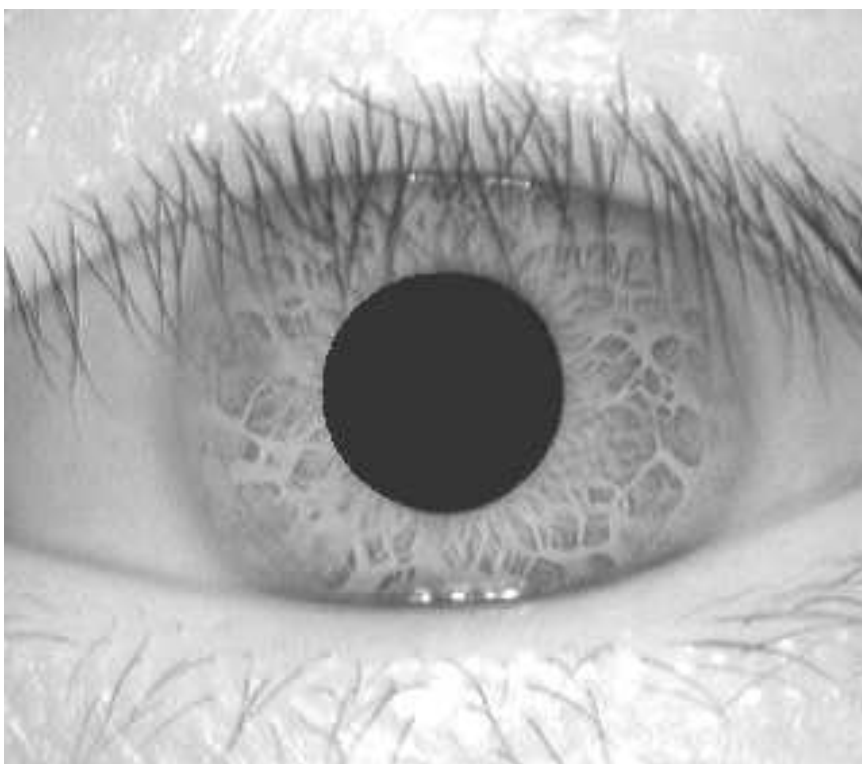
Figure 1.4: An iris image with eyelash and eyelid occlusions (image selected from the CASIA database [17]).

specular reflections. Inside the iris region, it is obvious that the illuminating light is reflected and captured by the camera. These specular reflections constitute a major source of distortion, and therefore should be eliminated, in order to make the iris recognition more accurate.
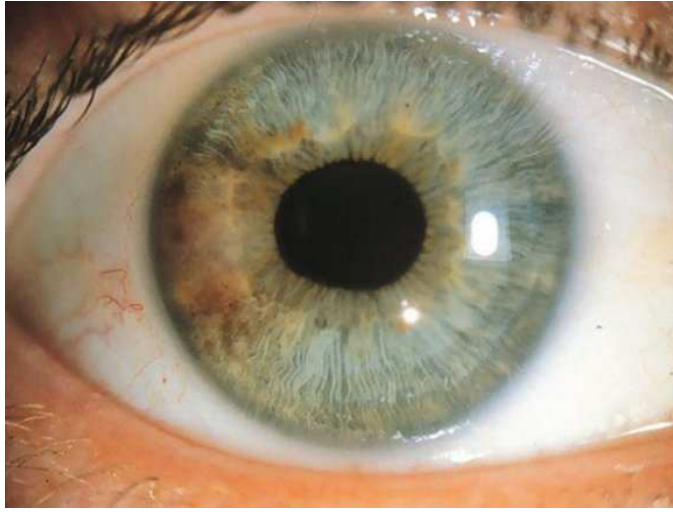
Figure 1.5: An iris image with specular reflections (image adapted from [18]).

1.3.5   Noise Detection and Removal

Several noise detection methods have been proposed to remove the noise introduced by the eyelash occlusion, the eyelid occlusion and the specular reflections. Eyelash detection proposed by Kong and Zhang [19] is based on the following three criteria.

Separable eyelash detection with 1D Gabor filter

First, the iris image is convolved with a 1D Gabor filter defined in Equation 1.9

$$G(x, \mu, \sigma) = e^{-x^2/2\sigma^2} cos(2\pi\mu x) \tag{1.9}$$

in which μ is the frequency of the sinusoidal wave, and σ is the standard deviation of the Gaussian envelope.

Then, a pre-defined threshold K_1 is set on the filtered image I as in Equation 1.10. The pixels with intensity values smaller than the threshold K_1 are identified as eyelash occluded regions. The threshold value K_1 is not given in the reference [19].

$$G(x, \mu, \sigma) * I(x) < K_1 \tag{1.10}$$

Multiple eyelash detection with local intensity variance

A 5×5 window is defined, and the variance var of image I are calculated as:

$$var = \frac{\sum_{i=-2}^{2} \sum_{j=-2}^{2} \left(I(x+i, y+j) - M\right)^2}{(2N+1)^2 - 1} \tag{1.11}$$

in which M is used to represent the mean of the image gray-scale intensities.

When multiple eyelashes are overlapping with one another, the local variance decreases from when there is no overlapping. By setting a threshold on the local variance with another pre-defined value K_2, the areas of overlapped eyelashes could be discovered.

Connective criterion

With our prior knowledge, we know that the eyelash is a continuous line instead of unconnected points. If a detected eyelash point is singled out as independent with no connection to another eyelash or eyelid pixel, then this point is removed from the candidates of potential eyelash pixels.

Specular reflection

Beside the eyelash detection algorithm, Kong and Zhang also presented one way to locate the specular reflection points, including strong reflections and weak reflections. Strong reflection points are located by setting a threshold K_3 on the iris pixel values.

$$I(x, y) < K_3 \tag{1.12}$$

For the transition area from the strong reflection to the surrounding iris region, the reflection intensities are relatively weaker, and they are still considered as noise instead of genuine iris pixels. A statistical test based on a normal distribution of intensity values is used. These intensity values are employed in this case to locate these weak reflection points. However, it lacks proper evidence to prove that the intensity values follow a normal distribution.

1.4 Size-invariant Unwrapping and Representation

1.4.1 Daugman Rubber Sheet Model

In order to accomplish a size-invariant sampling of the authenticate iris pixel points, John Daugman applied a rubber sheet model to map the sampled iris pixels from the Cartesian coordinates to the normalized polar coordinates.
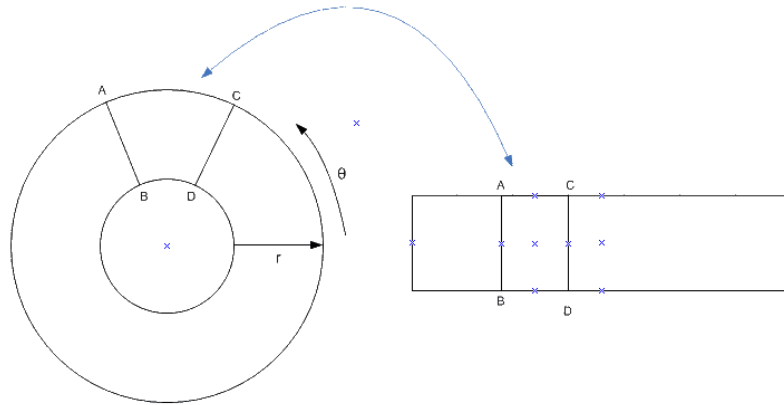
Figure 1.6: Daugman rubber sheet model.

Along the radial direction, the sampled intensity values are lined up corresponding to a column in the normalized polar scale. Similarly, the concentric circumferential circles in the Cartesian coordinates become rows of pixels in the polar coordinates.

The mapping functions from the Cartesian coordinates (x, y) to the Polar coordinates (r, θ) are as follows:

$$x(r, \theta) = (1 - r)x_p(\theta) + rx_i(\theta) \tag{1.13}$$

$$y(r, \theta) = (1 - r)y_p(\theta) + ry_i(\theta) \tag{1.14}$$

(x, y) represents the pixel location of the point in the Cartesian coordinates. (x_p, y_p) represents the pixel location of the point on the radius on the boundary of pupil circle. (x_i, y_i) represents the pixel location of the point along the radius on the boundary of iris circle. (r, θ) represents the corresponding coordinates in the unwrapped polar coordinates. r is the radial distance from the pixel to the boundary of pupil circle, and θ is the rotated angle from the starting radius.

The sampled iris feature points are uniformly distributed along a set of concentric circles. Moreover, there are more feature extraction schemes for the subsequent recognition process in a rectangular scale.

The rubber sheet model transfers the iris region from the circular Cartesian scale to the rectangular polar scale. When these two circle centers are located in the same pixel point, the sampled points are uniformly distributed across the iris region, as shown in Fig 1.7.

If the center of the iris circular boundary and the center of the pupil circular boundary are different from each other, the feature points are sampled non-uniformly within the iris region. First, a series of sampling lines are emitting from the center of the pupil circle, and rotating along the circumferential direction for 360°. Then a fixed number of sampled points would be taken inside the iris region along each sampling line, as shown in Fig 1.8.
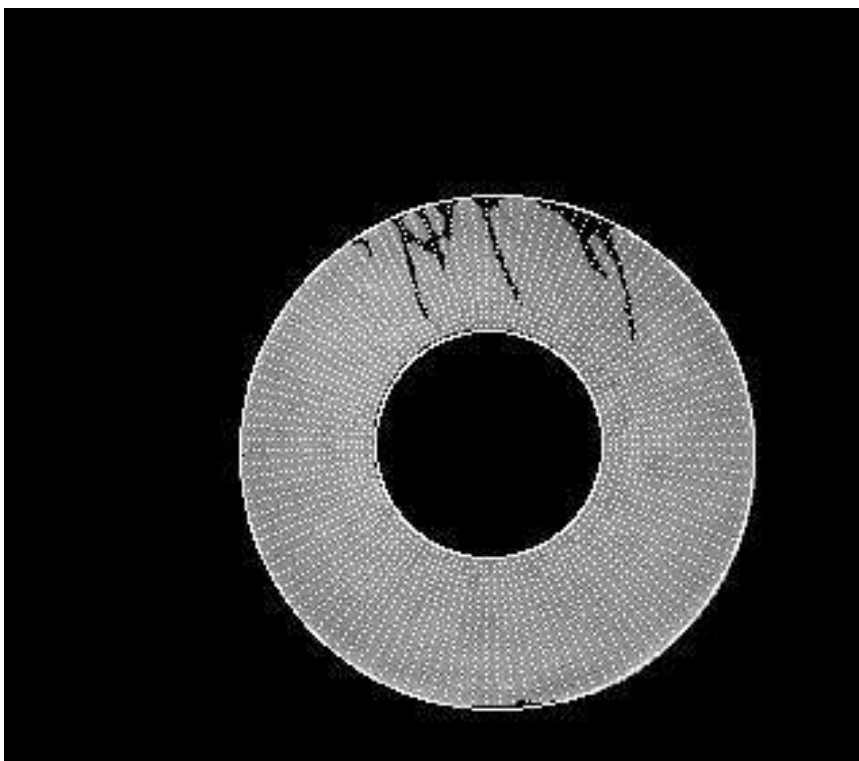
Figure 1.7: Uniform feature points sampling with the rubber sheet model.
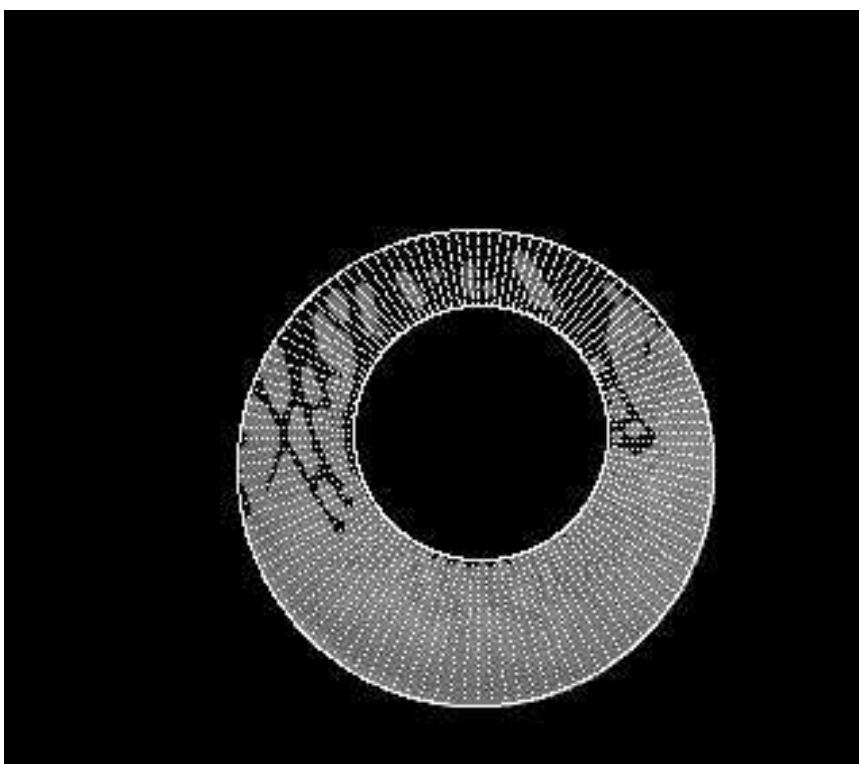
Figure 1.8: Feature points sampling with displaced pupil and iris centers.

1.4.2   Wildes Image Registration

The Wildes system is using an image representation technique, mapping the original iris image $I_a(x, y)$ to a base image $I_d(x, y)$ that minimizes the energy difference between the two images. The energy is defined as [13]:

$$\int_x \int_y I_d(x, y) = I_a(x - u, y - v)^2 dx dy \tag{1.15}$$

Here the mapping function $(u(x, y), v(x, y))$ is employed to calculate the image intensity values (u, v) from the original pixel value (x, y), as is used in Equation 1.15 for calculating the energy difference.

The similarity between the two coordinates could be calculated as the difference between the original coordinates and a scaled rotated version:

$$\begin{pmatrix} x' \\ y' \end{pmatrix} = \begin{pmatrix} x \\ y \end{pmatrix} - sR(\phi) \begin{pmatrix} x \\ y \end{pmatrix} \tag{1.16}$$

in which s represents the scaling factor and $R(\phi)$ represents the rotation transform matrix.

As a result, the aligned image after the registration has a uniform distribution of iris image sample points, and it is suitable for the subsequent feature extraction with the Laplacian pyramid.

1.4.3   Boles Virtual Circles

Boles and Boashash proposed to utilize a set of virtual circles from the iris region for representation before the feature extraction [20]. Before the comparison of iris images, the pupil and iris circular boundaries are first detected for both images, using standard techniques like the Hough transform. Then the images are scaled and mapped to the size-invariant circular templates that have uniform iris boundaries and pupil boundaries. In other words, the image pixels are aligned to the same circular positions. If it is a one-to-many comparison, the largest diameter of all image sets would be taken as a reference image, other images are scaled to the reference image before extracting the virtual circle sets. Using the center of the pupil region as a reference point, a set of virtual circles between the pupil boundary and the iris boundary are selected.

On each virtual circle, N points are selected uniformly as the feature points. N is an integer power of two, because the subsequent feature extraction uses the dyadic wavelet

transform to find the zero-crossings along the circle as the feature vectors.

This representation with virtual circles is essentially the same to the Daugman rubber sheet model, because both models take the feature points along the concentric circles which spreads within the iris region between the iris and the pupil circular boundaries.

1.5 Feature Extraction

Using different image representation techniques from various systems, the iris image features are extracted from the gray-scale image intensity values before the pattern comparison procedure. The uniqueness and variability are the key to successful personal identifications, in order to distinguish between templates.

1.5.1 2D Gabor Filter

The Daugman system applies a series of 2D Gabor wavelets to the isolated iris region in the normalized polar coordinates (r, θ). The Gabor filter could be seen as a Gaussian envelope multiplexed by a series of sinusoidal waves with different scales and rotations. Here the Daugman system uses the same function to explore the local intensity correlation of iris images in the space and frequency domains [7]. The filter wavelet is specified as:

$$H(r, \theta) = e^{-iw(\theta-\theta_0)} e^{-(r-r_0)^2/\alpha^2} e^{-i(\theta-\theta_0)^2/\beta^2} \tag{1.17}$$

in which α and β are used to specify the multi-scale 2D wavelet size. ω represents the wavelet frequency, which is inversely proportional to α and β. (r_0, θ_0) represents the center location of the frequency selective filter bank.

A collection of feature points are sampled from the original iris image in the Cartesian coordinates. These feature points are mapped, or in other words, unwrapped into a matrix representation in the normalized polar coordinates according to the Daugman rubber sheet model. Then the set of Gabor filter banks are applied to this matrix template and the template is decomposed into a set of complex coefficients h at each location (r_0, θ_0):

$$h = \int_r \int_\theta I(r, \theta) e^{-iw(\theta-\theta_0)} e^{-(r-r_0)^2/\alpha^2} e^{-i(\theta-\theta_0)^2/\beta^2} r dr d\theta \tag{1.18}$$

in which r and θ represent, respectively, the dimensions along the radial and circumferential directions in the normalized polar coordinates.

The complex domain is divided into four phases, and each phase is represented by two binary bits. After the Gabor feature extraction, a complex feature matrix is generated from the image. For each complex feature value h, two binary bits (h_R, h_I) are used to represent phase information at the pixel location. And the binary phase pairs from the entire image are combined into a binary feature template for pattern comparison and decision making. The Hamming distance is calculated between two binary feature templates to evaluate their closeness of match.
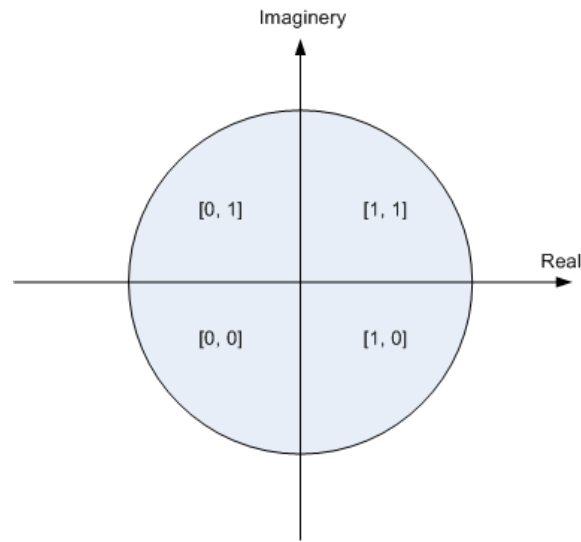
Figure 1.9: Gabor phase feature representation [7].

With different parameters selected for the Gabor decomposition, the phase encoding and feature extraction repeatedly process the iris region. One set of Gabor filter bank will extract one pair of complex phasors over each feature point. With k sets of Gabor filter banks applied to an unwrapped image template of $M \times N$ matrix, a binary phase feature matrix of $2kM \times 2kN$ would be extracted as the binary iris template for the Hamming distance calculation.

1.5.2 Laplacian of Gaussian filter

Compared to the Gabor filter wavelets used by the Daugman system, the Wildes system employs a Laplacian of Gaussian filter G to extract the features from the iris image [13]. The filter G is defined as:

$$G = -\frac{1}{\pi\sigma^4}(1 - \frac{\rho^2}{2\sigma^2})e^{-\rho^2/2\sigma^2} \tag{1.19}$$

in which ρ is the distance from the Gaussian center to the image point along the radius, and σ is the standard deviation of the Gaussian filter.

The segmented image I in the Cartesian coordinates is filtered with the Gaussian filter G to construct a Laplacian pyramid. First the image I is convolved with the filter G, and then down-sampled by 2 to generate the first filtered image g_1. Subsequently, each filtered image g_k is generated by convolving the previous one g_{k-1} with filter G, then down-sampled by 2, as shown in Equation 1.20.

$$g_k = (G * g_{k-1})_{\downarrow 2} \tag{1.20}$$

Each level of the Laplacian pyramid is generated according to Equation 1.21.

$$l_k = g_k - 4G * (g_{k+1})_{\uparrow 2} \tag{1.21}$$

in which l_k is the kth level of the Laplacian pyramid [21].

In the Wildes system, these different levels of Laplacian pyramids are combined into the feature templates of the iris images. During the pattern comparison, the normalized correlation is used to compare two iris feature templates to calculate the closeness of match and thus make the decision of classification.

1.5.3 Log-Gabor filter

Brady *et al.* presented a model to explore the effectiveness in coding the information in natural images [22]. The use of the Log-Gabor filter is examined to encode the spatial, frequency and orientation information in an image. He pointed out that Daugman system uses the Gabor filter for feature extraction, which is mostly efficient in the Cartesian coordinates.

However, the unwrapping process maps the iris pixel intensities from the Cartesian coordinates to the normalized polar coordinates. This transfer changes the relative spatial distribution among iris pixels, and therefore partially destroys some of the ability of the Gabor filter in extracting and compacting the spatial and frequency information.

Brady *et al.* proposed the Log-Gabor function to counterbalance the effect produced by the polar-mapping. The frequency response of the Log-Gabor function is:

$$G(f) = e^{-[log(f/f_0)]^2/2[log(\sigma/f_0)]^2} \tag{1.22}$$

in which f_0 represents the center frequency and σ represents the bandwidth of the filter.

With an unwrapped iris matrix representation, each row of pixel intensities corresponds to a ring of pixels centered at the pupil center. The Log-Gabor filter is applied to the 1D image vectors to extract the phase feature templates.

Since the normalization process is warping the iris region from the circular shape to the rectangular matrix, or from the Cartesian coordinates to the normalized polar coordinates, the spatial relationship along the concentric sampling rings is different from the spatial relationship along the radius. As a result, 2D Gabor filter feature extraction mechanism mixes the relative spatial relationship when it multiplexes over the normalized polar scale. In other words, 2D Gabor filter applies a symmetric Gaussian envelope to the normalized polar image representation which is not supposed to be treated evenly between radial and circumferential directions. On the other hand, the 1D Log-Gabor filter extracts the feature vector from each row of the normalized matrix representation, which avoids mixing the relative position information between the radial and the circumferential directions.

1.5.4 Zero-crossings of 1D wavelet

In the Boles and Boashash system, the dyadic wavelet transform is applied to preprocess the image intensity vectors, and uses the zero-crossings from the decomposed signals as the feature vectors for pattern matching [20].

A series of virtual circles are sampled from the gray-scale intensity iris images. Each circle is centered at the centroid of the pupil and represented with a 1-dimension signal vector $f(n)$. The iris signal vector $f(n)$ is sampled with a resolution of N. N is chosen to be an integer square as $N = 2^j$, to make it convenient for the subsequent dyadic wavelet decomposition. Then, the 1-dimension image vector $f(n)$ is decomposed with a set of dyadic wavelets at different resolutions. The locations of the zero-crossing points are used as the feature vectors.

The dyadic wavelet transform of signal $f(n)$ is defined as:

$$W_{a,b}f(n) = \sum_{n=-N}^{N} f(n)\frac{1}{a}\psi(\frac{n-b}{a}) \tag{1.23}$$

$\psi(\frac{n-b}{a})$ represents the dyadic wavelet function. a is a scalar, and b is a translation parameter to specify the size and position of the mother wavelet. The dyadic wavelet is defined as the second derivative of smoothing function $\theta(n)$, which is not specified in the reference.

1.5.5   Haar Transform

Lim *et al.* proposed to use the Haar transform [23] to extract the compact and efficient feature vectors. They used a relatively small number of feature values to effectively distinguish and classify iris images. The same unwrapping method is used in the preprocessing as the rubber sheet model by John Daugman. After the iris region is unwrapped into the normalized polar coordinates, a collection of feature points are sampled from the original iris image, with 450 feature points along the circumferential direction and 60 feature points along the radial direction. Then, the Haar wavelet decomposition is applied to this rectangular iris region of 450×60 matrix, as shown in Fig 1.11:
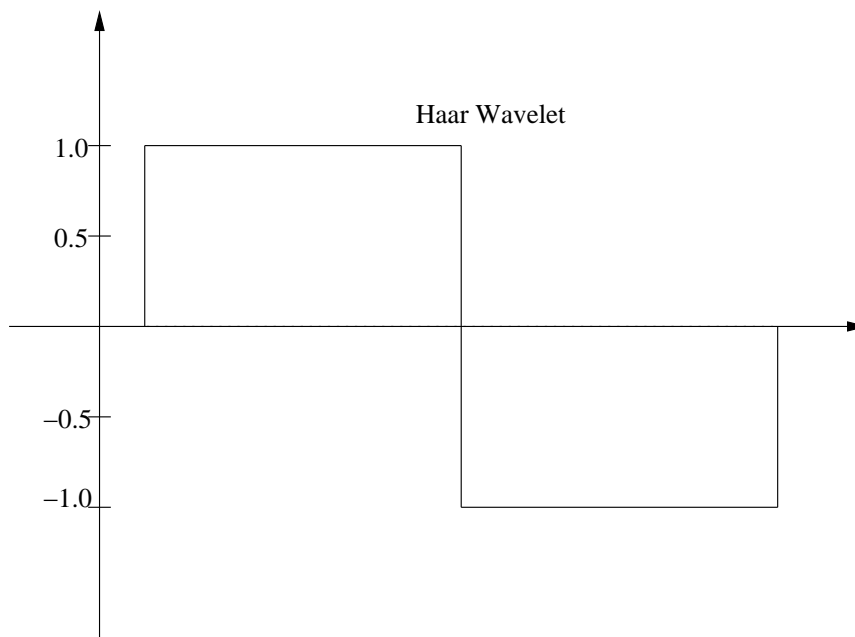
Figure 1.10: Haar basis wavelet [23].

There are wavelet decompositions from high-pass filters and low-pass filters along the vertical and horizontal directions. Four decompositions are applied, and the fourth HH component, with a size of 28×3, is comprised of 84 coefficients. The 84 coefficients
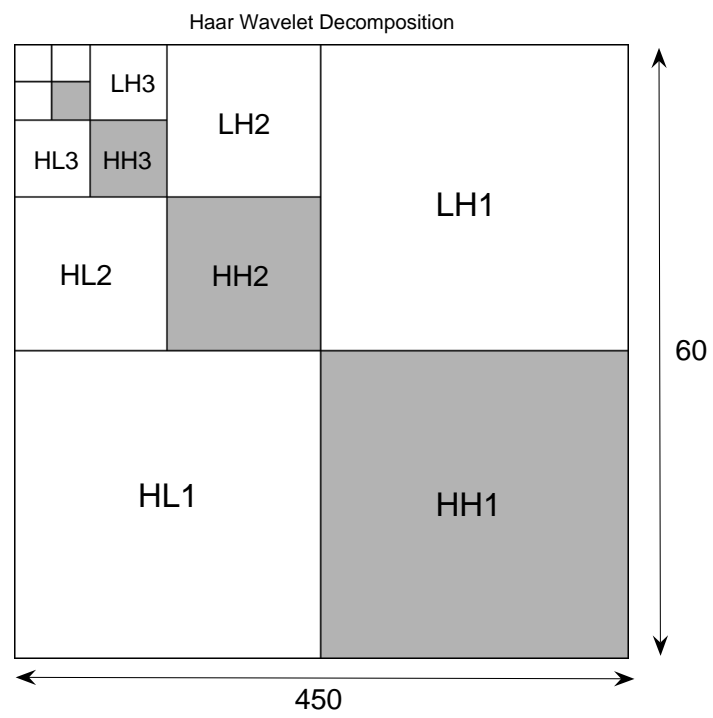
Figure 1.11: Wavelet decomposition with the Haar transform [23].

combined with the average values of the other three HH components, together make up the 87 feature coefficients. The 87 feature coefficients are within the range of -1 and 1, in which the signs of the coefficients are taken as the binary feature template.

The Haar wavelet feature extraction is compared to the Gabor feature extraction for evaluation [23]. The comparison are conducted over 200 people, with 30 images taken per person. The Haar wavelet feature templates are classified with a neural network, and it shows that the Haar feature vector of size 87-bit gives a slightly better recognition rate than the Gabor feature vector of 256-bit. At the same time, this feature extraction scheme reduces the computation cost by using feature templates of smaller size.

1.5.6 2D Hilbert transform

Using the same representation or unwrapping process as Daugman rubber sheet model, Christel Tisse *et al.* [24] presented a method of using 2D Hilbert transform to extract the features from the normalized rectangular iris images. The concept of the analytical signal is used here:

$$z_x(t) = x(t) + jHx(t) \tag{1.24}$$

in which $z_x(t)$ is the 1-D complex feature vector generated from original signal $x(t)$, and H stands for the Hilbert transform.

Similarly, the 2D version of the Hilbert transformed image is constructed, called analytical image, and calculated the instantaneous phase and the emergent frequency. Then, the complex phase information is taken as the iris feature template, in the same way as the Gabor transformed phase template in the Daugman system.

1.6 Distance Measure and Identification

With various feature extraction schemes, an iris image is transformed into a unique representation within the feature space. In order to make the decision of acceptance or refusal, a distance is calculated to measure the closeness of match. In iris recognition systems, such distance measures include the Hamming distance (HD), the normalized correlation (NC) and the weighted Euclidean distance (WED).

1.6.1 Hamming Distance

The Daugman algorithm [7] calculates the difference between individual patterns as a measure of statistical independence. With the encoded binary phase feature vectors, the Hamming distance between any two iris templates is defined in Equation 1.25.

$$HD = \frac{\| (template_A \otimes template_B \cap mask_A \cap mask_B \|}{\| mask_A \cap mask_B \|} \tag{1.25}$$

in which $template_A$ and $template_B$ represent the two encoded iris feature matrices. $mask_A$ and $mask_B$ are two binary masks, with the locations of the identified noise pixels marked with binary '0' and the rest of the mask with binary '1'. $\otimes$ is the logical XOR operator comparing bit by bit, and $\cap$ is the logical AND operator taking the common area of the valid iris regions.

Therefore, the Hamming distance calculates the pattern difference with a bit-by-bit comparison. For iris templates from the same eye, their statistical independence and the Hamming distance tend to approach zero, while two different iris templates tend to have a Hamming distance of 0.5. As a result, by setting a threshold on the Hamming distance between iris templates, a decision could be made about whether they come from the same eye or not, thus achieving the personal identification.

1.6.2 Normalized Correlation

The Wildes system employs the normalized correlation between two encoded iris images to measure their closeness of match.

The normalized correlation is defined as:

$$NC = \frac{\sum_{i=1}^{n} \sum_{j=1}^{m} (p_1[i,j] - u_1)(p_2[i,j] - u_2)}{nm\sigma_1\sigma_2} \tag{1.26}$$

in which p_1 and p_2 are the two encoded iris templates of size $n \times m$, u_1 and u_2 are the means of the images p_1 and p_2, and σ_1 and σ_2 are the standard deviations of the images p_1 and p_2.

1.6.3 Weighted Euclidean Distance

The Euclidean distance is one way of defining the closeness of match between two iris feature templates. It is calculated by measuring the norm between two vectors. For

the weighted Euclidean distance, another factor is taken into consideration because the percentage of decision-making varies in different dimensions.

Y. Zhu *et al.* [25] tried to use the weighted Euclidean distance to evaluate the closeness of an unknown iris template to a template in the existing database, defined as:

$$WED = \sum_{i=1}^{N} \frac{(f_i - g_i)^2}{\delta_i^2} \tag{1.27}$$

in which f is the unknown iris template to be matched and g is the iris template in the existing database to be compared with. i is used to denote the index of features in the templates, and δ is the standard deviation of the ith feature in template g.

Similar to the Hamming distance, the weighted Euclidean distance is another distance metric within a biometric system. In a complete system, the designer would have to interpret the metric to achieve identification or verification. In the Wildes algorithm, the iris template g with a minimum WED to the template f is identified to be from the same subject.

1.7   Evaluation Metrics

1.7.1   Genuine and Imposter Distributions

The genuine imposter distributions plot the normalized histogram of the matching metric, in this case the WED between the feature templates, according to whether or not they belong to the same subject.

The genuine histogram would be all the distances within the same class, while the imposter histogram would be all the distances between different classes. The genuine distances should be smaller to represent the closeness of two iris templates. The imposter distances should be generally bigger than genuine distances so that they could be classified with an appropriate threshold. The genuine and imposter distributions are represented by functions $f(x)$ and $g(x)$, which would be used to calculate the false match rate and the false non match rate.

1.7.2   False Match Rate and False Non Match Rate

Performance of an iris recognition system could also be evaluated with the variability among iris feature templates: within subject variability and between subject variability.

The within subject variability sets the limit for minimum false non match rate and the between subject variability sets the limit for minimum false match rate [26].

Given the genuine and imposter distributions as described before, another method, the false match rate (FMR) and the false non match rate (FNMR) curve could be plotted to evaluate the iris recognition system. With the above functions $f(x)$ and $g(x)$, the intra-class and inter-class comparisons between the feature templates could be represented with the genuine and imposter distributions. The x-axis is the direction along which the WED distances between iris feature vectors are plotted, and the y-axis is the percentage of WED distances that fall into that range. Then the FMR and FNMR could be calculated as Equation 1.28 and Equation 1.29 [27, 28]:

$$FMR(\tau) = \int_{\tau^-}^{\infty} f(x)dx = 1 - \int_{-\infty}^{\tau^+} f(x)dx \qquad (1.28)$$

$$FNMR(\tau) = \int_{-\infty}^{\tau^-} g(x)dx \qquad (1.29)$$

The threshold τ is varied within a range in the above calculations, and a series of corresponding FMR and FNMR values are generated. These match and non-match rate pairs are plotted in one graph of FNMR against FMR. The FNMR-FMR graph directly illustrates the trade-off between the false reject rates and the false accept rates, made with varying threshold τ. From a 100% reject to a 100% accept, the curve sweeps across the range of all possible thresholds τ during the identification process. An effective biometric system typically has a FNMR-FMR curve that extends from the position $(1,0)$ to $(0,1)$, and the curve in between warps towards the axes. In other words, the smaller is the area surrounded by the x-axis and y-axis, the better performance it achieves. FNMR-FMR graphs have been used extensively to evaluate the performance of a biometric system, and it is termed as detection error tradeoff (DET) in other occasions. The DET curve has been used in this thesis to evaluate the performance of iris recognition algorithm. One such example is shown in Fig 3.3.

1.7.3 Rank-1 Identification Rate

In iris recognition systems, a feature template is extracted from the acquired iris image, and compared to all other feature templates within the database by certain distance measurement, such as the Euclidean distance. Then the identification decision is made based on this distance, in other words, the closeness of match. Typically the smallest

distance is taken as the match. The decision based on the smallest distance is considered as the Rank-1 match, and the percentage of the correct matches among all comparisons is the rank-1 match score.

The Daugman system [7] uses the Hamming distance as the comparison metric. The smallest Hamming distance is considered as the right match. In the Wildes system [13], the WED is used as the comparison metric.

In this thesis, the Log-Gabor filter is used for the feature extraction, and the Hamming distance is used as the decision making metric. Therefore, among all cross-comparisons between the feature templates, the smallest Hamming distance is used to indicate a match. The percentage of such correct matches among all comparisons is the rank-1 identification rate.

1.7.4   Cumulative Match Curve

Cumulative match curve (CMC) is another way to evaluate the performance of a biometric system. It plots the cumulative match score against the rank, in other words the percent of images identified below the rank [29].

In the case of iris recognition, each feature template is compared to all other feature templates in the database. A complete set of distance metrics are generated, among which the smallest one is taken as the closest match in the class. Among all the comparisons, the rank-1 match score would be the percentage of the correct matches or identifications if using the smallest distance to determine the subject that the iris template belongs to. Similarly, the rank-2 match score would be the percentage of correct matches if using the second smallest distance as the correct match. So on and so forth, a series of match scores could be calculated against the ranks.

1.8   Independent Performance Evaluations

The theoretical analysis about the iris recognition technology claims that the texture pattern phase complexity has a 244 dimensions of freedom, and a discriminant entropy of $3.2bits/mm^2$ [30], which gives it very low error rates in personal identification.

However, for any emerging biometric technology to be accepted by the community, it typically requires an independent party to perform the evaluations, design the protocols, collect the data sets, supervise the tests and analyze the results [31]. There exist widely accepted standards and framework about how to design a biometric testing protocol,

how to collect data sets and minimize evaluation bias [32].

Over the years, the evaluations of iris recognition algorithms and systems has been done on various databases and population groups to acquire large scale results. The metrics like the FNMR and FMR, the detection error rate curve (DET) are used to indicate the level of accuracy of iris recognition systems.

Most recently, three independent evaluations with various iris recognition systems including hardware, software, image sensors, were performed by three institutions: the International Biometric Group (IBG), the Authenti-Corp and the National Institute of Standards and Technology (NIST).

1.8.1   Meta-analysis of Iris Recognition System

The meta-analysis was performed to compare the performances of three independent experiments. Three parties evaluated the iris recognition systems individually and separately. Each party collected an iris image database for its own experiment. The iris database included a collection from 29000 to 100000 images. The iris recognition algorithms that they evaluated were mostly modified versions of the Daugman system, except the algorithm from the IriTech Inc, which was claimed to be proprietary [11].

To compare the algorithms and systems, these evaluations utilized various metrics, such as the false accept rate and the false reject rate, the transaction time, the enrollment and acquisition failure rate. The meta-analysis used the results from all three independent evaluations, compared the FNMR at a common operating point of FMR = 0.001. It showed that all the tested iris recognition systems achieved very high identification rates, strong inter-operability and repeatability [10].

1.8.2   Iris Recognition Study 2006 (IRIS06)

The Iris Recognition Study 2006 (IRIS06) was funded by the US Department of Justice, the National Institute of Justice and the Department of Homeland Security. It was performed by the Authenti-Corp and lasted from December 2005 to early 2007 [12].

Authenti-Corp performed the evaluations of three up-to-date commercial iris recognition systems. Over 29000 iris images were acquired from around 300 people that demographically represented the US population. The images were taken according to the ISO/IEC 1994-6 standard within 15 minutes to 6 weeks periods, and under the supervision of their BETH systems (Biometric Evaluation Test Harness). The algorithms used for feature extraction and pattern matching were derived from the Daugman algorithm.

Their experiment findings include:

- The three-attempt failure to enroll (FTE) rates for all three systems are under 3.39%, and the true match rate reaches as high as 99.7% within a confidence interval of 95%.

- Multiple images are acquired from the same subject with up to six weeks period between the samples. The difference in acquisition time has very little impact on the system performance.

- There exists a tradeoff between the verification accuracy and the transaction time. A higher accuracy generally requires longer transaction time, and a low transaction time usually accompanies a higher error rate.

- Eyeglasses and the ambient lighting conditions have a direct influence on the iris image quality, and therefore have an impact on the recognition performance.

- All three systems perform the best when the subjects gaze upwards, rotate the head (ear-to-shoulder) within a 20° range, and stand within the designated distance.

At the same time, the IRIS06 project presented some future work to solve:

- How do iris image quality parameters influence the recognition performance?

- How to better understand the intra-individual correlation factor?

- Why do genuine iris image pairs fail to match sometimes?

1.8.3   Independent Testing of Iris Recognition Technology (ITIRT)

The ITIRT experiment was funded by the US Department of Homeland Security for border control and security access consulting. The test was performed in July 2004 on several state-of-the-art iris recognition systems [33]:

- Iridian KnoWho OEM SDK

- LG IrisAccess 3000

- Oki IRISPASS-WG

- Panasonic BM-ET300

Within the experiment period, over 100000 iris images were acquired at different times, with different devices. These images were taken from 1224 people of different ethnic and age groups. The image templates were compared and generated the false accept rates (FAR) and the false reject rates (FRR), the failure to enroll (FTE) and the failure to acquire rates (FTA). The feature extraction and matching algorithm used in those experiments was a generic version of the Daugman algorithm, and the same algorithm is used to test all of the four hardware systems.

The FNMR at FMR of 0.001 was used as one of the indicators of error rates. The Panasonic BM-ET300 image sensor achieved a FNMR of around 0.014. The Oki image sensor achieved a FNMR of around 0.03 at an FMR of 0.001. And the LG image sensor achieved a FNMR of around 0.038 [10].

1.8.4 Iris Challenge Evaluation (ICE 2006)

The Iris Challenge Evaluation 2006 (ICE2006) [11] was jointly funded by the US Department Homeland Security (DHS), the Federal Bureau of Investigation (FBI), the National Institute of Justice (NIJ) and the Technical Support Working Group (TWSG). It was a large-scale, independent testing and evaluation of iris recognition technologies.

The tested algorithms included:

- The CAM-2 from the University of Cambridge

- The SG-2 from Sagem-Iridian

- The IRTCH-2 from Iritech Inc.

The first two algorithms, the CAM-2 and the SG-2, were essentially the same based on the Daugman algorithm, and the IRTCH-2 is a proprietary algorithm from Iritech Inc.

There were 59558 images acquired from 240 subjects, including 29056 images from the right eyes and 30502 images from the left eyes. These images were further divided into 30 smaller data-sets. Each data-set was evaluated individually with various algorithms. The evaluations were also performed separately between the left and right eyes, and then the statistical results were combined for the subsequent analysis. All images were taken under the same controlled sampling condition and illumination, and they were of a high resolution at 480×640 pixels.

The experiment used the FRR at a FAR of 0.001 as a major evaluation metric for the statistical analysis. Among the three algorithms, at a FAR of 0.001, the smallest interquartile was a FRR of 0.09 and the largest interquartile was a FRR of 0.26. The Sagem-Iridian (SG-2) iris algorithm showed a relatively better performance with a FRR interquartile range of 0.011 to 0.014 at a FAR of 0.001 [11].

In terms of execution time needed to evaluate the database, the CAM-2 algorithm took 6 hours, and SG-2 and IRTCH-2 algorithms took about 300 hours.

1.9 Summary

Like any other biometric systems, an iris recognition system is a pattern recognition system that performs personal identification by "establishing the authenticity of a specific physiological or behavioral characteristic possessed by the user" [34]. Over the years, the iris recognition systems, from sensor technologies, to algorithms design, have been improved dramatically. Still, several issues need to be addressed and further understood. This thesis investigates the possible methods and solutions to improve the system performance of iris recognition with low quality iris images.

1.9.1 Database and Open Source Software Used

In this thesis, the CASIA iris image database [17] is used for the testing and experimentation. The CASIA database consists of 689 iris images that are acquired from 108 subjects with NIR cameras. All iris images in this database are gray-scale bit-map images, with the resolution of 320×280. The 108 subjects correspond to 108 different eyes, and we use each subject to represent one specific class of iris images. Each class consists of 6 or 7 iris images taken from the same eye.

In our test of iris recognition with low quality iris images, a subset database of 327 iris images are selected from the original CASIA database. These 327 images have regions that are partially occluded by eyelashes. All experimentations are conducted over these 327 iris images, including the eyelash detection, the circular localization, the covariance feature extraction, the Fourier magnitude feature extraction and the progressive segmentation.

One open source Matlab code framework was implemented by Libor Masek and Peter Kovesi [35], and new algorithms could be added into this framework for further investigation. The software is based on John Daugman's iris recognition algorithm, including the

segmentation, the normalization, the Gabor filter based feature extraction and the Hamming distance based pattern comparison. The different methods and experiments that we developed are implemented within this open source software framework by adding new functions, algorithms and libraries.

1.9.2   Eyelash and Eyelid Occlusions

Low quality images include the images with eyelash occlusions and eyelid occlusions. A typical example of such occluded image is shown previously in Fig 1.4. The upper eyelid and eyelashes have covered a significant portion of the iris, which introduce distortions from the ideal iris pixel intensity values. Moreover, the feature encoding process of these erroneous pixel values give erroneous feature values not only for these pixel locations, but also for adjacent pixel locations, because the feature extraction schemes involve the correlation calculation within the regional and global iris image, in both the frequency and spatial domains.

To solve the issue of eyelash occlusion, we developed an algorithm to detect the eyelash locations. With the eyelashes identified, the iris image pixels between these eyelashes are utilized, and the occluded iris regions are eliminated from the cross-comparison between image templates. The resulting DET curve showed improved error rates in most of the FMR range.

1.9.3   Erroneous Localization of Circular Boundaries

The first step in the iris recognition is to localize the iris region, typically surrounded by the iris and pupil boundaries. These two circular boundaries are usually detected using techniques like the Sobel or the Canny edge detector with the Hough transform. The large amount of iris image variations sometimes give errors during the circular segmentation, as observed in our examination. Fig 1.12 shows an example of the localization of the iris boundary with a large offset.

The circular parameters are corrected by sampling selected edge points and fitting to circular contours. The system with the corrected circular parameters is then compared to the one without the circular parameter correction to impact of erroneous circular localizations on the iris identification. The rank-1 identification rate, the DET curve, and the cumulative match curve have shown marginal improvement.
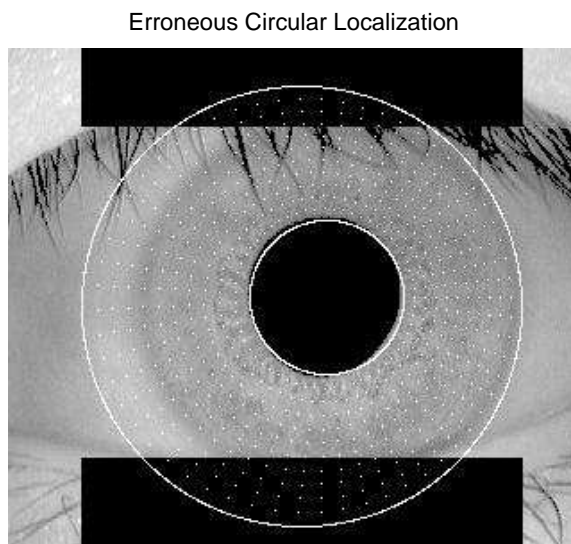
Figure 1.12: Erroneous circular localizations of iris and pupil boundaries.

1.9.4 Rotational Invariant Feature Extraction

Currently, in most feature extraction algorithms [7, 13, 20, 23, 24], the feature extraction procedure generates different feature templates when the iris images are rotated. Therefore, extra measures have to be taken to compensate the rotation offsets during the image acquisition and segmentation. For example, the Daugman system uses the rubber sheet model to transfer the rotational offset to a row-wise circular shifting in the normalized polar scale template. Then multiple comparisons between these shifted iris templates are calculated, among which the smallest Hamming distance is chosen as the one representing the closest match.

Two methods of feature extraction to explore the possibility of rotational invariant iris recognition systems : one based on the covariance features and one based on the Fourier transform magnitudes. The linear discriminant analysis was modified and used to classify and distinguish the covariance features for identification. The other algorithm is based on one-dimensional Fourier transform on the unwrapped iris image vectors, and two-dimensional Fourier transform on the entire unwrapped iris matrix templates. These features are classified with the Euclidean distance. The 1-D Fourier features achieve a 78.2% rank-1 identification rate, and the 2-D Fourier features achieve a 77.68% rank-1

identification rate. The performances from these two methods are not as good as the method with the Gabor feature extraction, and the main reason is the loss of the phase information when the Fourier magnitudes are calculated.

1.9.5 Information Content and Performance

A common assumption about an iris recognition system is that more valid iris image information contributes to a higher and better system performance for recognition.

We conducted tests to examine the quantitative relationship between the iris image content and the identification performance: the band-limited segmentation and the feature point sampling resolution. The selected area of iris region is gradually increased for the segmentation and for the subsequent inter-class and intra-class comparisons. It is shown that during a critical range of iris image area, the system performance improves rapidly. Overall, it proves in this thesis that the iris recognition with low quality iris images could provide reliable and satisfactory system performance.

Chapter 2

Eyelash Detection and Enhanced Segmentation

2.1 Eyelash and Eyelid Occlusions

One of the problems inside an iris recognition system is the use of incomplete or distorted iris images, as well as the noise introduced during processing, such as unsuccessful segmentation, unwanted eyelash and eyelid pixels.

There are some algorithms that try to bypass the eyelash occlusion by selecting an iris boundary within the real iris region, such as the one presented by A. Poursaberil *et al.* [36]. We consider this method unacceptable since it avoids eyelashes by eliminating both the eyelashes and certain iris regions. Furthermore, it changes the relative sampling distribution of the feature points.

In this chapter, we developed an algorithm to obtain more detailed iris image area while eliminating distortion as much as possible. This approach is based on the enhanced iris segmentation with an advanced eyelash detection algorithm.

The advantages of this approach include:

- Fewer artifacts and distortion

- More iris pixels from iris images for the recognition

The masked images are normalized and encoded by the Log-Gabor filter. Then the encoded iris feature templates are classified with the Hamming distance as used by the Daugman system [7]. The result shows that the enhanced segmentation decreases the

genuine distances and the error rates, which effectively increases the robustness of the recognition system.

2.2 Enhanced Segmentation

2.2.1 Pupil and Iris Circle Localization

The pupil and iris regions are assumed to be of circular shape. The Hough transform, combined with standard edge detection techniques, has been used widely for the circular localization. Our approach is also based on the Hough transform to detect the circular boundaries in iris images.

Image enhancement

The original image $F(x, y)$ goes through a recursive smoothing processing as shown in the block diagram in Fig 2.1 [37, 38]. The low pass filter (LPF) applied here is a 9×9 Gaussian filter. In each step, the output image from the previous Gaussian LPF is the input of the next Gaussian LPF. $A_n(x, y)$ represents the low pass filtered image in each step. $H_n(x, y)$ represents the subtraction of the images before and after low pass filtering. s is the scalar to control the contrast level in the final enhanced image $F'(x, y)$. The recursive filtering procedure is repeated until $A_{n-1}(x, y) \ominus A_n(x, y) \approx 0$.
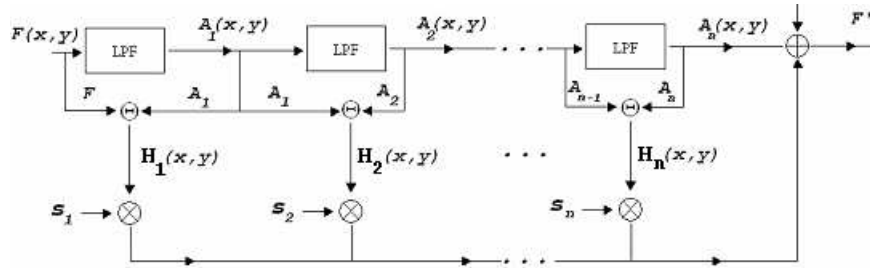
Figure 2.1: Non-linear image enhancement, adapted from [38].

The Gaussian filtering is computed in the gray-scale intensity space, while the addition $\oplus$, subtraction $\ominus$ and multiplication $\otimes$ are defined in the logarithmic mapping space. In other words, the images are mapped into logarithmic space before the addition, subtraction and multiplication, and inversely mapped into the gray-scale intensity space after these operations.

The mapping function from the gray-scale image $F(x, y)$ into the logarithmic space is defined in Equation 2.1:

$$\Psi(F(x,y)) = log(\frac{255 - F(x,y)}{F(x,y)})$$ (2.1)

Based on this mapping approach, the addition operation of images A and H in the logarithmic space is defined in Equation 2.2:

$$A \oplus H = \Psi^{-1}(\Psi(A) + \Psi(H))$$ (2.2)

The subtraction operation of images F and A in logarithmic space is defined in Equation 2.3:

$$A \ominus H = \Psi^{-1}(\Psi(A) - \Psi(H))$$ (2.3)

The multiplication operation of an image A and a scalar s in logarithmic space is defined in Equation 2.4:

$$s \otimes A = \Psi^{-1}(s\Psi(H))$$ (2.4)

This recursive filtering procedure attempts to smooth and clean the distortions in the images, which makes it more accurate in the subsequent localization of the circular boundaries in iris images. Then the images with clean edges and contrasts are used for the segmentation, the feature extraction and the pattern comparison.

Here the smoothed image $F'(x, y)$ is used to search for the circular boundaries of iris and pupil regions. Once the parameters of these boundaries are located, the original iris image is used for the feature extraction and the subsequent processing.

Edge detection and the Hough transform

The contrast and edge enhanced image $F'(x, y)$ is used here to identify the spatial gradient map with the Sobel edge detector. Then the Hough transform is applied to the binary edge image to locate the iris and pupil circles. By polling through a series of circular parameter sets corresponding to the circular center and radius, the circular parameter set that goes through the most number of edge points is taken as the most likely circular parameter set.

This approach is applied to find both the iris and pupil circles, with different area limits. First of all, the Hough transform polling is conducted over the entire image after edge detection. In this case, the iris boundaries are most likely those with the most amount of edge points located on the circular boundaries, and the detected circular

parameters indicate the center and radius of the iris circle. Then, the area of the Hough transform search is limited to within this iris circle, and the circle with the most amount of edge candidates would be the pupil boundary.

2.2.2   Eyelash Detection

The eyelash detection is based on local image statistics, and the eyelashes are divided into two groups: separable eyelashes and multiple eyelashes.

Separable eyelashes

Separable eyelashes could be in various directions: horizontal, vertical or diagonal. Therefore, four different convolution masks are used to detect these directional edges. The kernels are shown in Fig 2.2.

-1	-1	-1
2	2	2
-1	-1	-1

-1	2	-1
-1	2	-1
-1	2	-1

2	-1	-1
-1	2	-1
-1	-1	2

-1	-1	2
-1	2	-1
2	-1	-1

Figure 2.2: Separable eyelash detection kernels

The image is convolved with the kernel masks as:

$$R_i(x, y) = \sum_{m=-N}^{N} \sum_{n=-N}^{N} I(x - m, y - n)M(m, n) \tag{2.5}$$

in which I denotes the original image, and $M(m, n)$ denotes the convolution kernel of size (2N+1) by (2N+1).

Then a threshold is set on the mask response $R_i(x, y)$ to identify the possible eyelash locations. In our algorithm, a threshold of -200 is selected.

Also, a connective criterion must be satisfied for a candidate eyelash pixel to be valid [19], which means that a possible eyelash point is only valid when it is connected to other identified eyelash points in the surrounding pixel regions.

Multiple eyelashes

Local statistics are used to locate the regions with multiple eyelashes crossing over one another. The mean u_{bi} and variance v_{bi} of each $(2N+1) \times (2N+1)$ block are calculated from the original iris image I. Then the mean and variance values are compared to the predefined thresholds to find out the possible eyelash regions. In this experiment, the block is chosen to be size 5×5, and N equals 2.

$$u_{bi}(x,y) = \frac{1}{N^2} \sum_{i=-N}^{N} \sum_{j=-N}^{n} I(x+i, y+j) \tag{2.6}$$

$$v_b i(x,y) = \frac{1}{N^2} \sum_{i=-N}^{n} \sum_{j=-N}^{n} \left(I(x+i, y+j) - u_{bi}(x,y)\right)^2 \tag{2.7}$$

A similar connective criterion is also applied to the detection of multiple eyelashes. Each potential eyelash candidate pixel has to be connected to at least one other identified eyelash pixel in the surrounding region.

2.3 Iris Recognition based on Enhanced Segmentation

The iris image is unwrapped into a normalized polar scale template, according to the Daugman rubber sheet model. At the same time, the mask indicating the location of unwanted artifact pixels is also mapped from the Cartesian coordinates to the normalized polar scale.

2.3.1 Enhanced Segmentation

The traditional way of segmenting the iris image consists of locating the iris and pupil boundary circles, and the parabola of the upper and lower eyelids, using the Hough transform. Fig 2.3 is one of the original images from the CASIA database. Fig 2.4 shows the segmented iris region generated with the open-source software provided by Libor Masek *et al.* [35]. The performance evaluation is compared between the algorithm from Libor Masek *et al.*, which does not perform eyelash detection, and our enhanced segmentation with eyelash detection.

In Fig 2.4, the shaded regions on the top and bottom of the iris image are discarded as noise. The valid iris region utilized is the area surrounded by the iris circular boundary,
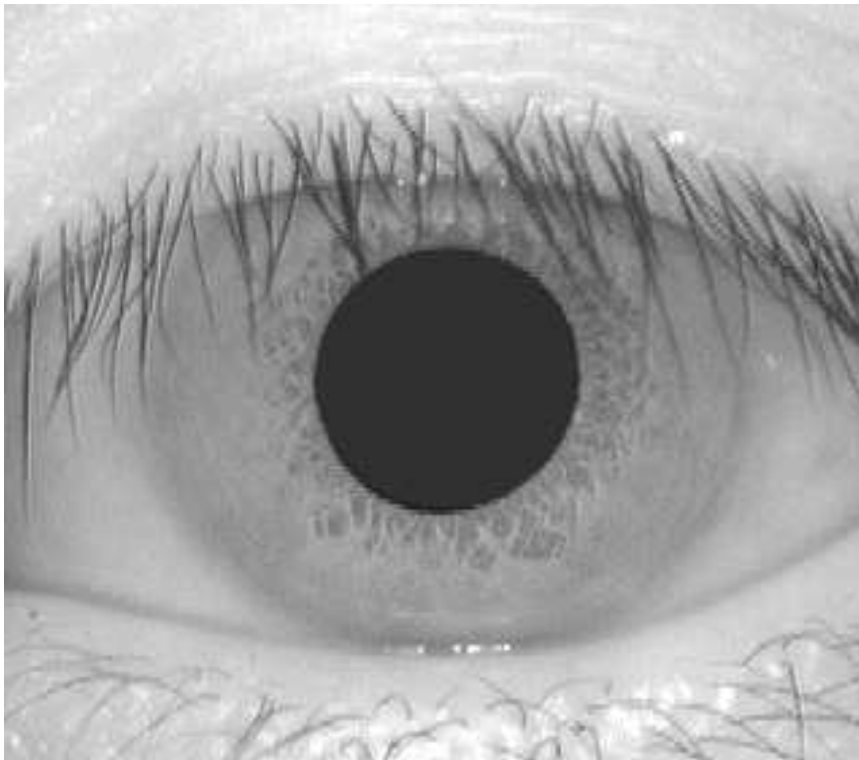
Figure 2.3: One sample iris image from the CASIA database [17]
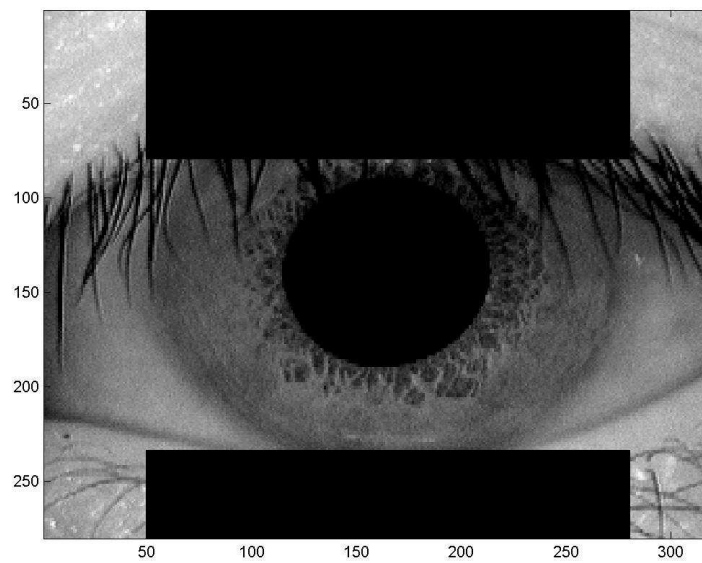
Figure 2.4: Segmentation using the Masek's algorithm [39].

pupil circular boundary and the two shaded areas. Instead, the average pixel intensity value of the valid iris region is filled into these shaded regions for the subsequent feature extraction.

Our proposed advanced segmentation aims to improve the result of Fig 2.4 by eliminating the eyelashes outside the mask, and identifying all the valid iris regions that would otherwise be discarded (the region that is covered by the dark mask in Fig 2.4).

With the above method of eyelash detection, the same image as Fig 2.4 is segmented as shown in Fig 2.5. In Fig 2.5, the eyelashes are detected, and the iris pixel locations occluded by the eyelashes are discarded. Meanwhile, the valid iris pixels between these eyelashes are kept for the subsequent feature extraction and the pattern matching. Therefore, it further reduces the unwanted noise region while revealing the iris region that is ignored by the Masek's segmentation.
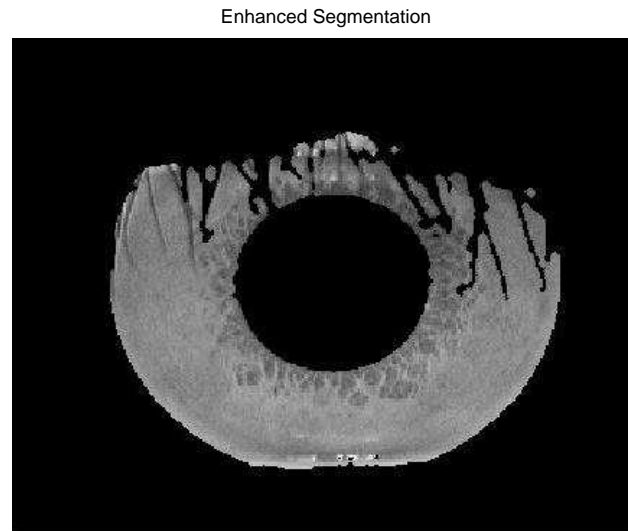
Figure 2.5: Enhanced segmentation with eyelash detection.

2.3.2   Unwrapping

The unwrapping involves mapping the segmented iris image into a rectangular polar scale matrix. The feature points are selected from the original image with a specified sampling resolution, like 20×120, which indicates that 20 feature points are selected along the radial direction and 120 feature points are selected along the circumferential direction.

The rubber sheet model [7] is proposed by John Daugman as a representation of an iris image, which makes it easy to use the Gabor filter to extract the binary feature templates for the pattern comparison.

This unwrapping model maps each point in the Cartesian coordinates (x, y) to the polar coordinates (r, θ), in which r represents the radial distance from the center of pupil circle, and θ represents the angular shifting from 0 to 2π.

The mapping function from the Cartesian to the polar coordinates is defined in Equation 2.8 and 2.9 [39]:

$$x(r, \theta) = (1 - r)x_p(\theta) + rx_i(\theta) \tag{2.8}$$

$$y(r, \theta) = (1 - r)y_p(\theta) + ry_i(\theta) \tag{2.9}$$

in which (x, y) represents the Cartesian coordinates, (r, θ) is the corresponding polar coordinates. (x_p, y_p) and (x_i, y_i) are the Cartesian coordinates for the two end points of the radius across the iris region, along which the mapped points are located. Fig 2.6 shows an example of the unwrapping process to generate the normalized polar scale representation.

The unwrapping according to this rubber sheet model compensates the distortions, like the displacement between iris and pupil centers. As a result, it gives a uniform sampling of the feature points across the iris region. Fig 2.7 and Fig 2.8 show the sampling process of both the iris image with the Masek's segmentation and with the enhanced segmentation. The white dots within the two circles indicate the points at which features are selected, including 20 points along the radial direction and 120 points along the circumferential direction.

For the iris region covered by eyelids, eyelashes, and other identified noise, they would be given an interpolated value before encoding. An averaged value of all other valid iris pixel values to interpolate the eyelash covered region [39] as is shown in Fig 2.9. A 5×5 averaging filter is used to generate the estimated pixel values at those regions as illustrated in Fig 2.10. The benefit of the second interpolation method is that it introduces relatively less sharp edges, and less distortion for the feature extractor. It is shown by comparing Fig 2.9 and Fig 2.10. In Fig 2.9, the artifact pixels are interpolated using a 5×5 averaging filter.

Then these two rectangular iris templates are convolved with the 1-D Log-Gabor filter to extract the binary feature templates, including the binary features for valid iris
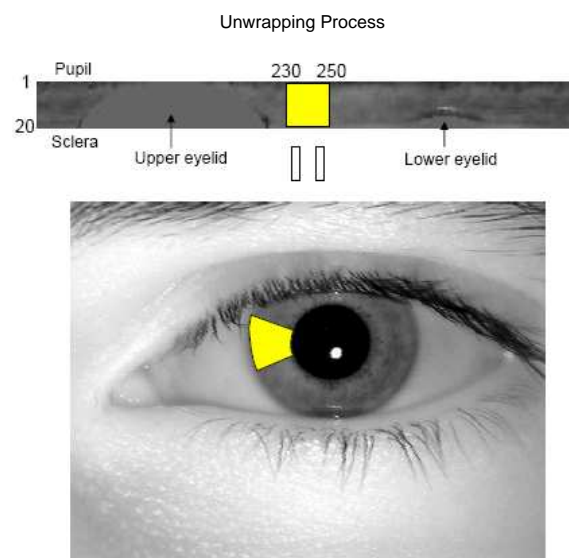
Figure 2.6: Rubber sheet model unwrapping, adapted from [40]. The yellow region in the original iris image is mapped to the rectangular yellow region between column 230 and 250 in the unwrapped iris template shown above.
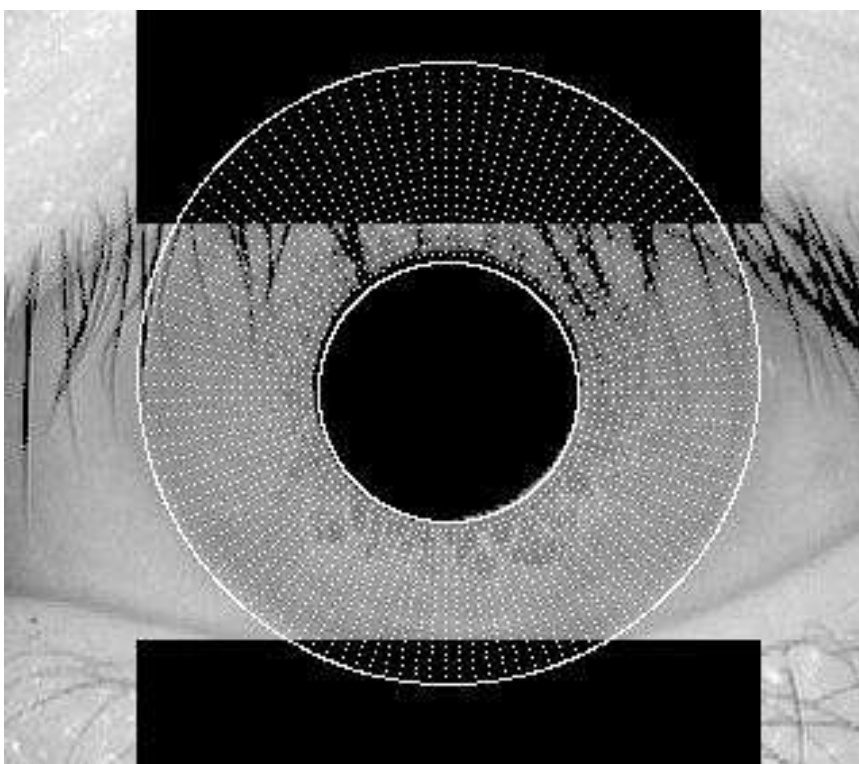
Figure 2.7: Sampling of the image with the Masek's segmentation.
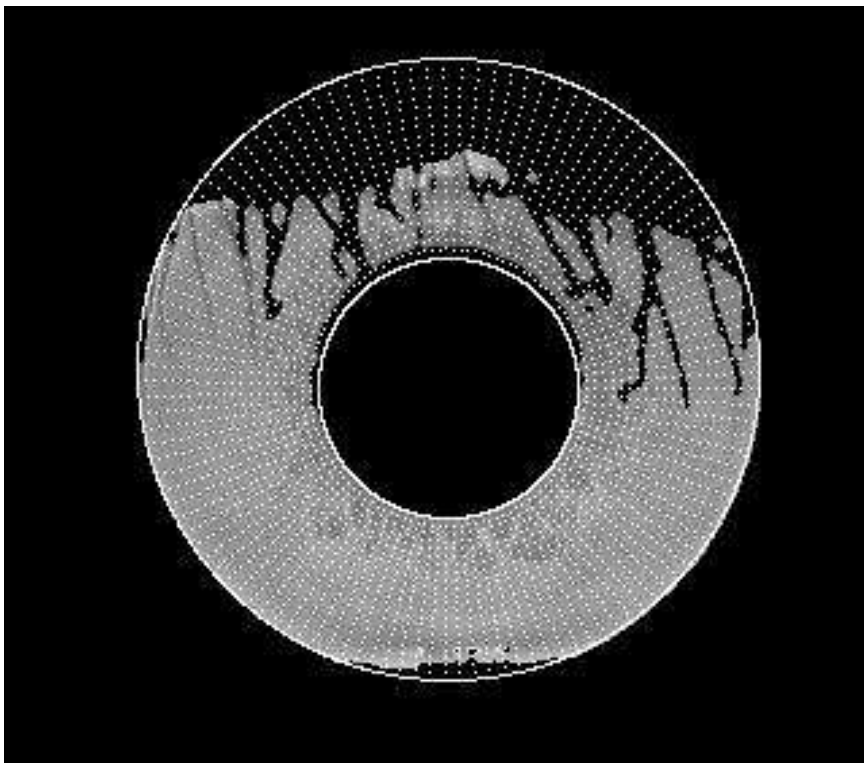
Figure 2.8: Sampling of the image with accurate eyelash detection.

regions and invalid interpolated regions, which will be masked out subsequently. The mask is a binary template that has the same size as the iris intensity pixel template. Examples are shown in Fig 2.11 and Fig 2.12. Inside the binary masks, the binary $0s$ indicates the locations of unwanted pixels in the iris templates, which would be used to discard these pixel features during the Hamming distance calculation.

Figure 2.9: Unwrapping of the Masek's segmented image. The segmented iris images are unwrapped into this rectangular image templates according the Daugman's rubber sheet model.

Figure 2.10: Unwrapping of the iris image with the eyelash detection.

The sampled points within the identified noise region will be marked, as indicated by the black shades in Fig 2.7 and Fig 2.8. After the unwrapping process, the noise points will also be marked in the polar coordinates, as explained above in terms of masks. Fig 2.11 and Fig 2.12 are the corresponding masks, indicating the locations of invalid and unwanted pixels, which are used to eliminate the noise during the Hamming distance calculation.

2.3.3 Feature extraction

The Log-Gabor filter is used as a feature extractor to encode the unwrapped iris images into binary templates. The frequency response of the Log-Gabor filter is represented in equation 2.10:

$$G(f) = e^{-\frac{[log(f/f_0)]^2}{2[log(\sigma/f_0)]^2}} \tag{2.10}$$

where f represents the frequency component of the image vector, f_0 represents the center frequency of the filter and σ gives the bandwidth of the Log-Gabor filter.

Figure 2.11: The binary mask for the Masek's segmentation. The binary $0s$ (black) indicate the existence of noise, and they are discarded from the Hamming distance calculation. Only the pixel values indicated by the binary $1s$ (white) are used for the Hamming distance calculation and the pattern matching.

Figure 2.12: The binary mask for the enhanced segmentation. It is shown that more accurate eyelashes are detected and discarded from the pattern matching.

Each row in the unwrapped iris template corresponds to one circle in the iris region in the Cartesian scale. The normalized iris image in the polar scale is convolved by the 1-D Log-Gabor filter, row by row. The output of the convolution produces one complex value for each pixel point, which is located in one of the four complex phase domains.

Fig 2.13 shows an image intensity vector in the normalized gray-scale image template. This normalized image template is convolved with the Log-Gabor filter to extract the feature vectors, and the corresponding real and imaginary components of the complex feature vector are displayed in Fig 2.14. In Fig 2.14, the blue line represents the real part of the feature vector along the pixel index and the red line represents the imaginary part of the feature vector. At each pixel location, a binary '1' is used to indicate a positive value, and a binary '0' is used to indicate a non-positive value. Therefore, each feature value is encoded with a binary pair. The binary pairs from the entire image make up the binary feature template, which is used for pattern matching with the Hamming distance.
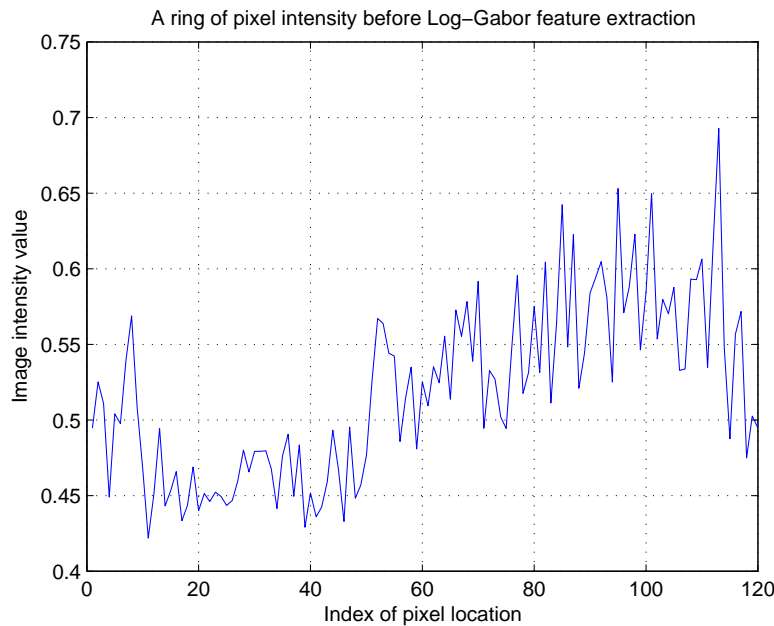
Figure 2.13: Iris image gray-scale intensity vector.

The quadrature phase information for each pixel point is represented by two binary values, indicating the complex convolved value in one of the 4 complex domains as shown previously in Fig 1.9. Thus, each iris image template of size $[M, N]$ is decomposed into a complex feature template of size $[M, N]$, which is further represented with binary phase template of size $[2M, 2N]$.
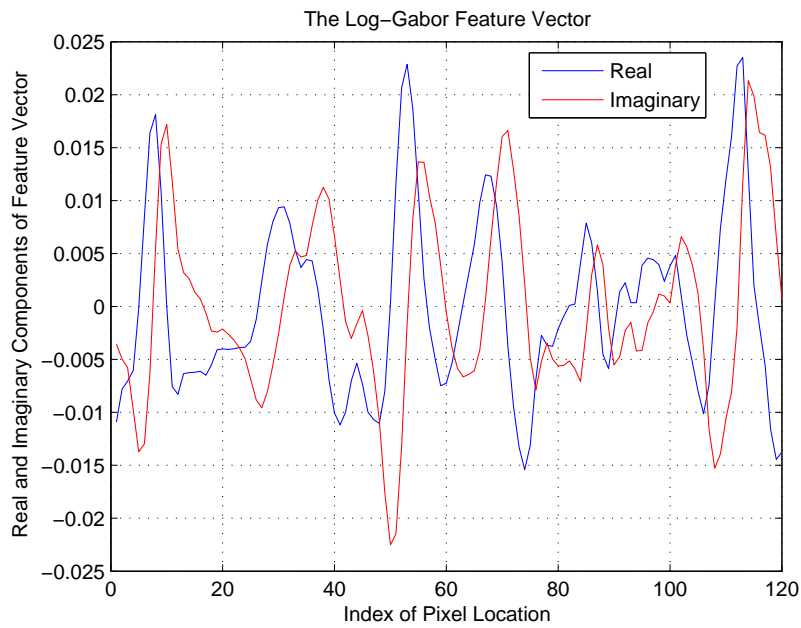
Figure 2.14: Real and imaginary components of Log-Gabor feature vector. The blue and red curves correspond to the real and imaginary components of the Log-Gabor feature vector respectively.

2.3.4   Pattern Recognition

In order to determine whether two iris feature templates are from the same subject, a distance measure is calculated based on the comparison between images of the same eye (intra-class comparison) and between images of different eyes (inter-class comparison). Overall, the intra-class comparisons have smaller distances than the inter-class comparisons.

The Hamming distance is defined previously in Equation 1.25. It is used to measure the closeness of match of the intra-class and the inter-class comparisons [7].

The templates to be compared are the encoded iris feature binary matrices. The masks are the corresponding binary masks, with the location of identified noise marked with binary 0s and the remaining image with binary 1s as shown in Fig 2.11 and Fig 2.12.

Note that the XOR operation is taken between two iris feature templates. Then the Hamming distance is calculated by averaging the XOR results from the common valid iris region indicated by the masks. The values within the noise area are discarded, including the noise marked by masks from both compared images. From all the cross-comparison Hamming distances of all iris templates, the minimum distance is selected as the right class to which the candidate iris image belongs.

Rotational invariance is compensated by circularly shifting the encoded iris templates along the row-wise direction, including both left and right shifting. Each row in the template corresponds to one circular contour in the original iris region. For a sampling resolution of 120 along the circumferential direction, a collection of 240 binary feature values are generated as the feature vector. Therefore in the feature templates, row-wise bit-shifting could compensate for the circular rotation in the original Cartesian coordinates.

2.4   Performance Evaluation

The CASIA database [17] is comprised of 689 gray-scale iris images in bit-map format. From the entire database, we select a group of 327 iris image that are partially occluded by eyelashes.

The detection error trade-off curve (DET) is generated by plotting the false non-match rate against the false match rate, as shown in Fig 2.15. Among the two plotted curves, the red curve represents the DET curve of the Masek's segmentation and the blue curve represents the DET curve of the enhanced segmentation with accurate eyelash detection.

The enhanced segmentation improves the recognition performance for most of the region except in very low FMR range.
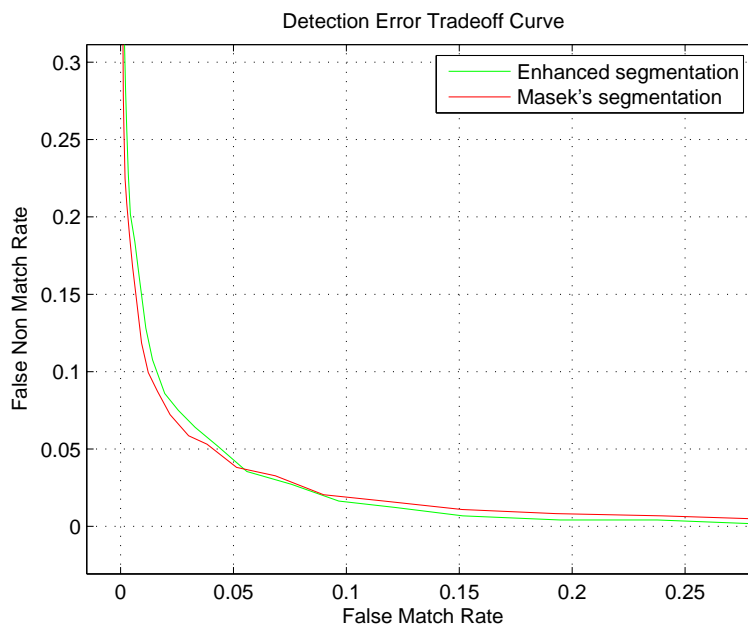
Figure 2.15: DET curve comparison. Performances are compared between the Masek's segmentation and the enhanced segmentation.

The DET curve with the enhanced segmentation has a lower error rate than the Masek's segmentation, except at very low FMR. In other words, we could say that with the enhanced segmentation, the match score is better within the whole comparison range.

The major reason for the improved match score is the extra iris image information that is utilized, as well as the artifact pixels that are discarded to minimize the distortion like eyelash and eyelid occlusions. In other words, the Masek's segmentation is too aggressive in eliminating the noise pixels. As a result, a lot of useful information and valid iris pixel points are discarded from recognition.

By using the advanced segmentation with additional valid iris pixels while eliminating invalid eyelashes or eyelids, the iris recognition performance is improved in the detection error trade-off curve. That is especially useful when the acquired iris images are noisy and distorted as a result of the camera tilting or lack of client cooperation.

Chapter 3

Improved Pupil and Iris Localization

3.1   Introduction

One potential problem in the iris recognition system is that the same algorithm and parameter settings are applied to a large amount of iris images in the database. Because of the large variation in image quality and patterns, the errors and offsets often occur during the processing, including the localization, the unwrapping, the feature extraction and the pattern matching.

During the procedure of iris localization, the pupil and iris boundaries are identified by fitting circles to the detected edge points. The Sobel edge detection with the Hough transform is used to find the circular parameters for the iris and pupil boundaries. From our experiments, the standard Hough transform generates a number of erroneous circular detections. These errors are due to the texture patterns with misleading circular edges from the eyelids and eyelashes that cause incorrect circular detections. One example is shown in Fig 1.12 in Chapter 1. The figure is generated from the open source code by Libor Masek *et al.* [35], in which the iris boundary is significantly offset from the true iris region.

Therefore, we investigated the impact of these erroneous circular detections on overall performance. A more robust and accurate circular localization algorithm could be developed, using recursive searching for decision making. Before that, it is valuable to know how much impact the erroneous circular detections have on the overall recognition performance.

Certain edge points along the circular boundaries are selected to fit into the circular parameters. The system performance is evaluated before and after correcting the circular

parameters. The test results show that an improved circular localization generates a improved system performance.

3.2 Standard Method of Circular Localization

The standard method to determine the parameters for a circle is the Hough transform combined with the edge detection. The edge detection method could be the Canny detector, the Sobel detector or other methods.

Our experiments are performed on a database from CASIA [17], from which 327 low-quality iris images are selected, particularly with eyelash or eyelid occlusions. These artifacts make it more difficult to accurately localize the circular boundaries, since the sharp edges from eyelashes are taken as pixel points over a circle. Among the 327 images, 15 images show significant errors in the circular segmentation, like Fig 1.12. There are 15 additional images having minor errors in the circular radius detection.

3.3 Correction to Circular Localization

The images with erroneous circular localizations are picked out for manual correction. The method we employed to find the correct circular parameters is to sample edge points over the circular contour and search for a circle that fits the most with these points.

A circle is defined by three parameters: the center coordinates (c_x, c_y) and the radius r. For all the points (x, y) on the circle, the relationship is defined as:

$$(x - c_x)^2 + (y - c_y)^2 = r^2 \tag{3.1}$$

To find the three parameters corresponding to the iris circular boundary, a set of N points are manually sampled on the iris circle: $(x_1, y_1)...(x_N, y_N)$. Then the Matlab simplex search method is used to find the optimal parameter combinations of (c_x, c_y, r) to minimize Equation 3.2:

$$min_{(c_x, c_y, r)} \sum_{i=1}^{N} \left| (x_i - c_x)^2 + (y_i - c_y)^2 - r^2 \right| \tag{3.2}$$

Similarly, by sampling N points on the pupil circles and do the same search as above, the optimal parameter sets could be found to localize the pupil boundaries.

3.4 Testing and Performance Evaluation

With all the corrected circle parameter sets from above, the new system performance is tested based on the rubber sheet model representation, the Log-Gabor feature extraction and the Hamming distance for decision making, which we have introduced in Chapter 3. Here we briefly describe it.

The newly corrected circular parameters are used to map the iris region from the Cartesian coordinates to the normalized polar coordinates. M by N feature points are sampled within the iris region, including M points along the radial direction and N points along the circumferential direction. Their coordinates are mapped according to Equations 2.8 and 2.9.

The unwrapped iris images are convolved with the Log-Gabor filter to extract the binary phase features. The Log-Gabor filter is represented in Equation 2.10.

The Hamming distance is calculated by the cross-comparisons of all iris feature templates to find the closest match for recognition. The method to calculate the Hamming distance is defined in Equation 1.25.

The algorithm is implemented within the open source software framework from Libor Masek *et al.* [35] and the same algorithm with corrected circular parameters. Two tests are examined, with two different sampling resolutions.

3.4.1 Test One with Sampling Resolution [10 60]

In each segmented iris image, 10 feature points are sampled along the radial direction and 60 points are sampled along the circumferential direction. Each iris feature template is compared to all other iris feature templates in the database in terms of the Hamming distance. The smallest Hamming distance is used to indicate a correct match, and the percentage of the correct matches is termed the rank-1 identification rate [Section 1.7.3].

Without the circular correction, the algorithm achieves a rank-1 identification rate of 72.47%. After the circular correction, the same algorithm achieves a rank-1 identification rate of 74.37%. The comparison of the cumulative match curves is shown in Fig 3.1.

While there is some improvement in the rank-1 identification rate, the genuine-imposter distributions look very similar to each other in Fig 3.2. The improvement is difficult to notice. It is expected that this correction will influence the genuine distributions at high distance regions.

The FMR-FNMR curves from both methods before and after circular correction are illustrated in one graph as shown in Fig 3.3. Again, they overlap with each other for the
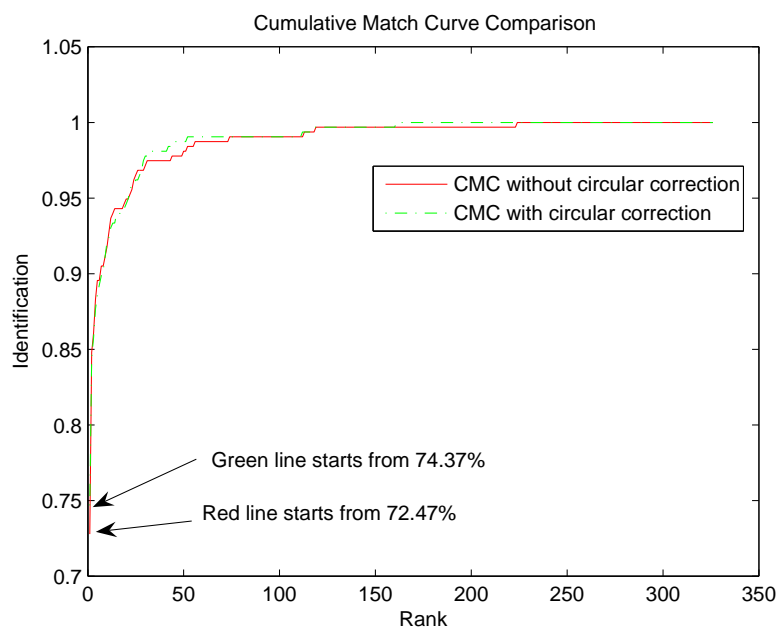
Figure 3.1: Cumulative match curve before and after the circular correction. Without the correction of erroneous circular localizations, it achieves a rank-1 identification rate of 72.47%. After the correction of the erroneous circular localizations, it achieves a rank-1 identification rate of 74.37%.
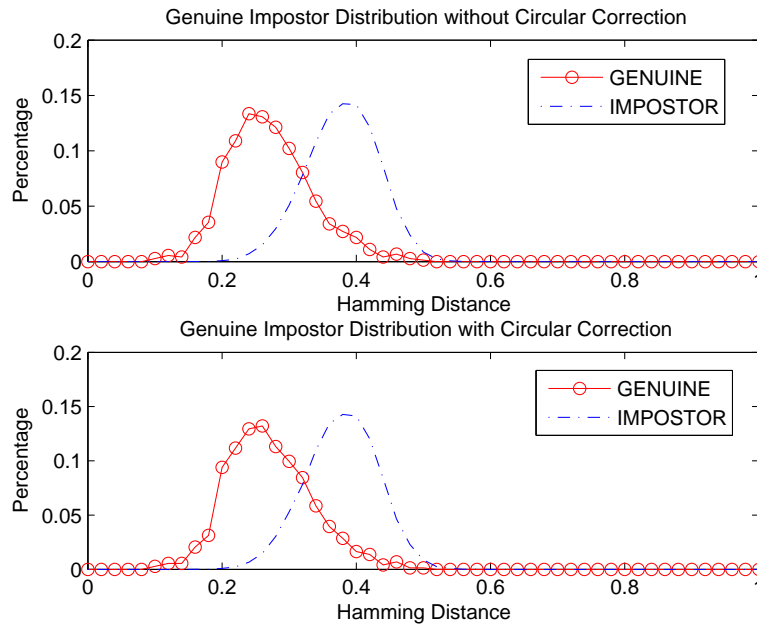
Figure 3.2: Genuine imposter curve comparison. The genuine imposter distributions before and after the circular correction are very similar.

majority of the curve, if viewed with a higher resolution in Fig 3.4.

3.4.2 Test Two with Sampling Resolution [20 120]

In this test, the method is using the same algorithm as above but with a different sampling resolution of the feature points. Instead of sampling 10 feature points along the radial direction and 60 points along the circumferential direction, a sample collection of 20 points along the radial direction and 120 points along the circumferential direction is utilized for the Log-Gabor binary feature extraction. Generally, the performance shows similar comparison results between the old circular segmentation and the corrected circular segmentation.

The rank-1 identification rate increases from 96.20% to 96.84%. In Fig 3.5, two cumulative match curves from before and after the circular correction are illustrated. The increase in the identification rate shows the positive effect of the corrected iris and pupil boundaries parameters. The relative improvement of 0.64% is smaller than the previous testing, because the recognition rate has already reached a very high level at this sampling resolution. Therefore, it approves that an enhanced circular localization
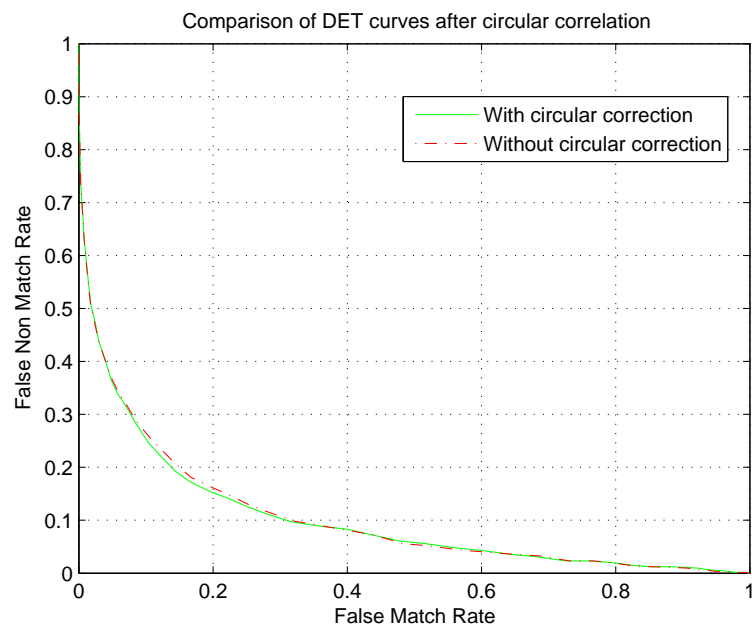
Figure 3.3: DET curve comparison. The red line represents the DET curve for the evaluation without correction of the erroneous localizations of the circular boundaries. The green line represents the DET curve after the correction of the circular localizations.
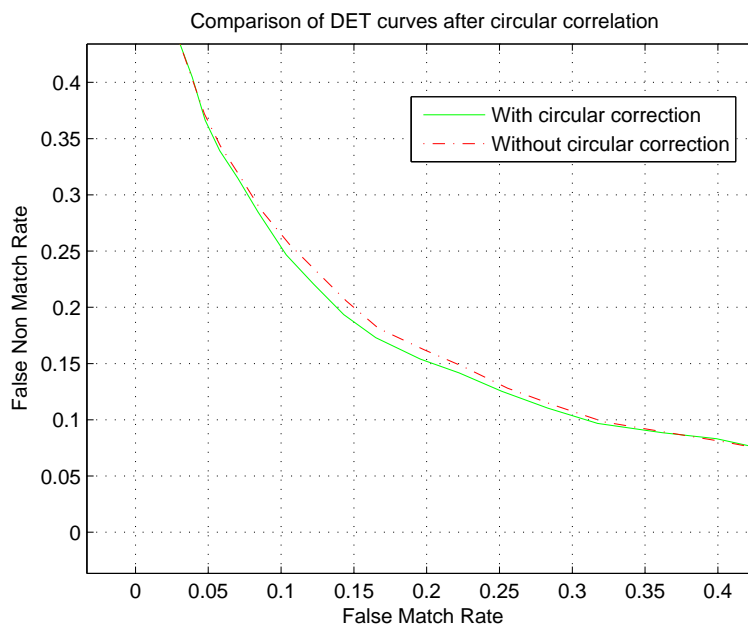
Figure 3.4: A higher resolution of Fig 3.3. An improvement in the DET curve is observed after the correction of the circular localizations in most of the FMR range.

has a positive impact on the system performance.

This relative improvement is small in the genuine imposter distributions, as shown in Fig 3.6. The genuine-imposter distributions of the system without the corrected circular segmentation are similar to the system with the circular correction.

Both FMR-FNMR curves are plotted together for comparison in Fig 3.7. The solid line represents the DET curve with no circular correction and the dotted line represents the DET curve after the circular correction. Two curves almost overlap with each other. If the graph is viewed with a higher resolution in Fig 3.8, it shows that the corrected circular localization gives better error rates in most of the range except at very low FMR.

3.5   Conclusion

From the two examinations and comparisons, the rank-1 rate, the DET curve and the CMC curve have shown marginal improvement in the system performance after the erroneous circular localizations are corrected. Overall, it provides an alternative to improve the robustness and performance in iris recognition, which is to increase the accuracy in the circular localization. This is essentially based on the same assumption as Chapter 3,
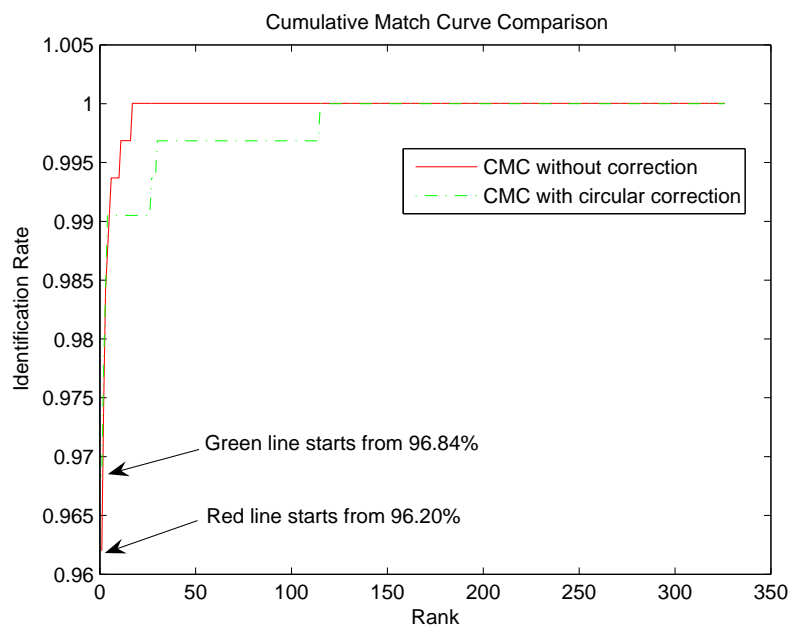
Figure 3.5: Cumulative match curves comparison with and without the circular correction. Without the correction of circular localizations, a rank-1 identification rate of 96.20% is observed. After the correction of circular localizations, a rank-1 identification rate of 96.84% is observed.
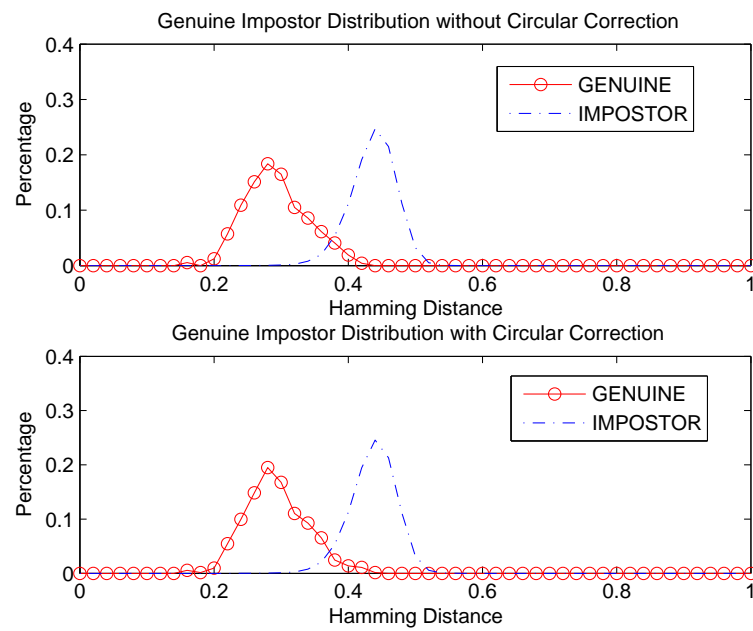
Figure 3.6: Genuine imposter distribution comparison with and without the circular correction.

which extracts more iris information by detecting the eyelash locations and utilizing the extra information between these eyelash occluded regions.
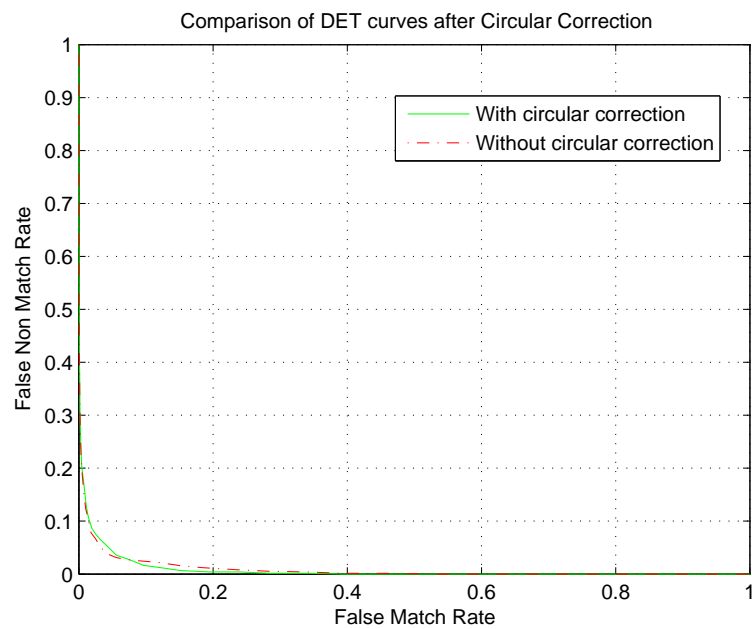
Figure 3.7: DET curves comparison before and after the circular correction. The red line represents the DET curve before the correction and the green line represents the DET curve after correcting the circular localizations. Two curves are very similar, and a higher resolution comparison is illustrated in Fig 3.8
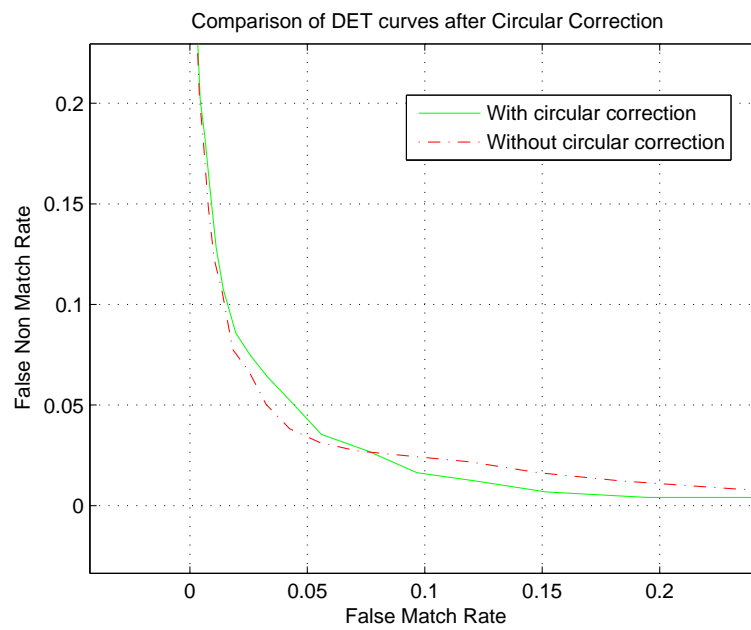
Figure 3.8: A higher resolution of Fig 3.7. It is shown that after the correction of the erroneous circular localization, the FNMR is improved in most of the FMR range.

Chapter 4

Covariance Feature and Fisher Discriminant Analysis

4.1 Introduction

In this chapter, a rotational invariant feature extraction method is developed, based on the cross covariances between the iris image pixel rings. A modified linear discriminant analysis is utilized to test the iris recognition performance. Experiments have been done on the CASIA database. Extended issues over the feature selection are also discussed. From the simulation, it is seen that the rotational invariance is achieved, but the classification capability of the linear discriminant classifier is limited. We try to explore the possible reasons and solutions.

4.2 Localization, Representation and Feature Extraction

4.2.1 Segmentation and Unwrapping

The circular boundaries of the iris and pupil regions are localized with the standard Hough transform. Artifacts like the eyelash occlusions are detected using the methods described in Chapter 2. Then, a normalized representation template in polar scale is generated according to the Daugman rubber sheet model [7].

4.2.2 Covariance Feature Extraction

The assumption for the covariance feature is based on:

- The iris image features are spatially distributed in the radial and circumferential directions

- The covariance of iris image pixels would be non-zero within the local region and close to zero outside the local region.

- Iris pixel intensities far apart have a random distribution, thus little correlations with each other.

After the process of segmentation and unwrapping, the iris region is mapped into a matrix with specified dimensions. Each row of pixel values corresponds to one ring in the iris image. Then, for each combination of row pairs, the covariances between different pairs of ring pixels are calculated and combined as one feature template:

$$cov(i,j) = \frac{1}{N-1} \sum ring(i) * ring(j) \tag{4.1}$$

where $cov(i,j)$ is the covariance between two iris pixel rings; i,j represents the index of each ring of pixel values; and N is the number of pixels across one ring of iris image.

Across the radial direction, the covariance between each pair of ring pixels are calculated as the feature point. All these feature points were combined together as one feature vector for the subsequent identification purpose.

4.2.3 Feature Selection

It is shown that the covariances between iris ring pixels have abundant feature information for identification. Similarly, the covariances between the same rings of iris image also contain a lot of features. In our method, a ring-ring covariance has the characteristic of the rotational invariance.

After the segmentation and the unwrapping, the circular rotation is transformed into a linear bit shifting of pixel matrix rows. The above procedure of calculating the covariance features generates a large number of feature vectors. Over the radial direction of 20 pixels, 400 possible combinations of ring pairs are generated. And during the calculation of the covariances between the pixel rings, each pixel ring could be circularly shifted to the left or right. Two rings of pixels could be rotated before calculating their covariances. Thus

over the circumferential direction of 120 sampled pixels, each pixel ring could be rotated by 0 to 60 bits before calculating the covariances, which give a lot more information about the iris regional image distributions.

Noise sources include the eyelash occlusion, the eyelid occlusion, and the specular reflections. The identified noise pixel intensities are set to zero, and they have no impact on the covariance feature vectors.

It is assumed that in an iris image, along the radial direction, pixels values close to each other should correlate more closely than those that are far apart. Therefore, the cross-covariances between closer rings should weigh more in terms of the classification capability. When choosing the feature points before the classification, we use the cross-covariance between two rings that are no further than a pre-determined limit along the radial direction.

For instance, the features calculated between rings within a bandwidth of 4 pixels is shown in Fig 4.1. Similarly, for an iris image with 20 rings of pixels, the bandwidth could be from 1 pixel, which is auto-covariance of each pixel ring, to 20 pixels, which include the covariances between all possible pairs of ring pixel values.

4.3 Fisher Discriminant Analysis

One image generates a feature vector of 400 values with a bandwidth of 20 pixels. So it becomes an issue about how to discriminate those features within the feature space or classify against an appropriate hyper-plane.

With the feature vectors to represent the iris images, we applied the modified fisher discrimination classifier.

4.3.1 Fisher Discriminant Analysis

With multi-dimension feature vectors, the traditional Fisher discriminant analysis (FDA) projects each high-dimension feature vectors into the Fisher classification space, then performs the identification based on a distance metric between the feature vectors in the Fisher space.

The search for the projection matrix is aimed at finding a projection plane that maximizes the distance between the means of two classes and minimizing the variance within each class [41].

If there are samples from two different classes, $x_1^1, ..., x_M^1$ and $x_1^2, ..., x_N^2$, the covariance

matrix within the classes S_W and the covariance matrix between the classes S_B are defined as:

$$S_W = \sum_k \sum_m (x_m^k - \bar{x^k})(x_m^k - \bar{x^k})^T \qquad (4.2)$$

$$S_B = (\bar{x^1} - \bar{x^2})(\bar{x^1} - \bar{x^2})^T \qquad (4.3)$$

in which x_m^k represents the mth feature vector in the kth class, $\bar{x^k}$ represents the mean of all feature vectors in k^{th} class, k represents the index of class, 1 or 2 in this case, and m represents the index of the feature vector in each class.

The projection matrix W is found based on the Fisher criterion [42] to maximize:

$$J(W) = \frac{W^T S_B W}{W^T S_W W} \qquad (4.4)$$

The optimal projection matrix could be computed by solving the generalized eigenvalue problem [42]:

$$S_B W = \lambda S_W W \qquad (4.5)$$

Thus, all feature vectors are projected into the Fisher space:

$$Y = W^T * x \qquad (4.6)$$

in which x represents the feature vector, W represents the projection matrix, and Y represents the projected vector in the feature space.

The conventional way to classify the feature templates is calculating the Euclidean distance between each vector Y, and make the decision based on the closeness of the projected vectors.

4.3.2   Modified Fisher Discriminant Analysis

In our examination, the Fisher discriminant analysis is modified for classification among multiple classes.

Moreover, the high dimension of the iris feature vectors results in the difficulty of finding a convergent inverse matrix of the within-class covariance matrix. The traditional Fisher discriminant analysis does not perform satisfactorily in this iris identification work.

Instead of projecting into one projection plane, each feature vector is projected into a high-dimension Fisher space. The iris images from the same class tend to form a

high-dimension spheres in this Fisher space, so we could use different Fisher spheres to represent different iris classes. And each iris image is classified based on its closeness to each iris Fisher sphere center.

The procedure is as follows:

- The within-class covariance matrix S_W is calculated from the feature vectors of all iris classes:

$$S_W = \sum_k \sum_m (x_m^k - \bar{x}^k)(x_m^k - \bar{x}^k)^T \tag{4.7}$$

  in which S_W represents the within class covariance matrix, x represents the covariance feature vector, k represents the index of iris image class, and m represents the image index inside each class of iris images.

- The singular value decomposition of S_W is calculated as:

$$[U, S, V] = svd(S_W) \tag{4.8}$$

  such that

$$S_W = U * S * V' \tag{4.9}$$

- The mapping matrix is generated from the covariance feature space to the Fisher classification space, with certain regularization applied:

$$M = S^{-1/2} * U' \tag{4.10}$$

  in which M is the mapping matrix from the covariance space to the Fisher space.

  The regularization aims to select the highest covariance feature values. Before the calculation of Equation 4.10, a regularization is done by selecting a limited rows or columns of the SVD matrix as $U = U(1:400, 1:100)$ and $S = S(1:100, 1:100)$.

- All image features are mapped from all possible classes into this newly-defined classification space:

$$F = M * x \tag{4.11}$$

in which F represents the corresponding feature vector in the Fisher space, M represents the mapping matrix from covariance space to the Fisher space, and x represents the originally covariance feature vector.

- For any iris image to be identified, the Euclidean distance is calculated between the feature vector to be identified and each feature vector template in the existing database:

$$D = norm[F_i - F_j] \tag{4.12}$$

in which D represents the Euclidean distance, F_i represents the iris feature vector to be identified, and F_j represents the feature vector in database to be compared with.

- Then the iris image is identified as belonging to the class, with the smallest Euclidean distance D.

4.4 Performance Evaluation

4.4.1 Database

The covariance feature extraction scheme with the Fisher discriminant classifier is tested on the CASIA database [17]. The 327 iris images are acquired from 108 eyes, with 6 or 7 images per subject. These images are segmented and normalized to generate the feature vectors. The classification is achieved by calculating the within-class covariance matrix S_W from these 327 feature vectors, and finding the the Fisher mapping matrix by using the singular value decomposition.

For the 108 eyes, the identification is done by comparing any one iris feature template to all other 326 feature templates, and the smallest weighted Euclidean distance is used to indicate the closest match. The identification results from the WED comparisons are tested and verified using the prior information from the database.

4.4.2 Evaluation Metric

Cumulative Match Curve

The cumulative match curve is plotted with the rank against the cumulative match score, indicating the percentage of the correct identifications below the specified rank [29].

The cumulative match curve is a derivative curve from the rank rate scores, in which the cumulative score at each rank is the sum of all match scores below or equal to the selected rank. Fig 4.1 illustrates the CMC graph for the iris recognition system using the covariance feature extraction with the Fisher discriminant analysis.

From the CMC graph, it is shown that the rank-1 identification rate is close to zero, which means the feature vectors extracted from the images of the same subject do not match close enough to be correctly identified. Therefore, the covariance feature combined with the modified Fisher discriminant classifier fails to classify the iris images properly. The reason is that the Fisher discriminant classifier does not have the capability to classify these covariance features. From the genuine imposter distributions, it is shown that the inter-class and intra-class feature distances fail to distinguish the iris classes.
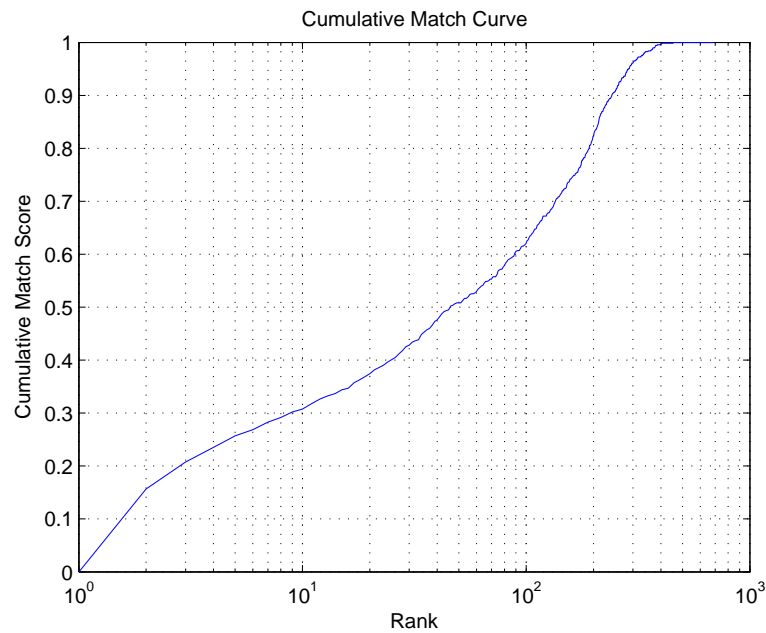

Figure 4.1: The cumulative match curve for the covariance features with the modified FDA. It fails to distinguish between the feature templates.

Genuine Imposter Distribution

The genuine imposter distributions plot the normalized histogram of the distance measurements between the feature templates, including the intra-class and inter-class comparisons.

In our test with 327 iris images, 106602 cross comparisons between the images are calculated including the genuine and the impostor distances, and the distributions are shown in Fig 4.2. The solid line is the histogram of the intra-class WED distances, and the dotted line is the histogram of the within-class WED distances. These two curves have a large amount of overlap, and their peaks of statistical distributions nearly merge. In other words, it is difficult to distinguish the two distributions by any threshold or correctly identify the iris feature templates.
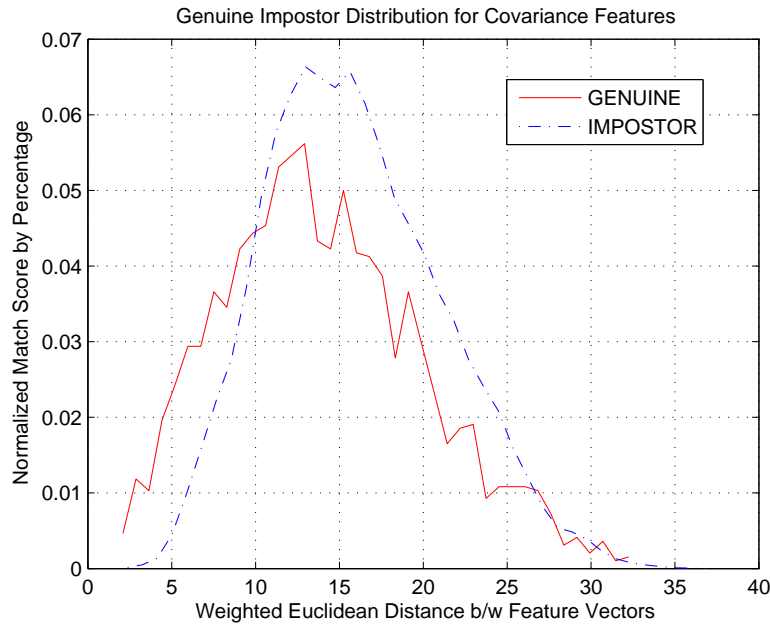

Figure 4.2: Genuine imposter distributions of the covariance features with FDA. The genuine distribution in red line and the imposter distribution in blue line are overlapping with each other. This algorithm fails to separate the genuine distribution from the imposter distribution.

FMR-FNMR Curve

The FMR-FNMR curve plots the percentage of the false acceptances against the percentage of the false rejections during the identification. It is sometimes termed as the detection error rate curve.

$f(x)$ and $g(x)$ are used to represent the genuine and imposter distributions of the intra-class and inter-class comparisons between the covariance feature templates. The x-axis shows the index of each covariance feature distance, and the y-axis is the percentage

of the distances. Then the FMR rate and FNMR rate are calculated in the same way as described in Chapter 2, as in Equations 1.28 and 1.29.

In the test of the covariance feature combined with the Fisher discriminant analysis, the FNMR-FMR curve is plotted in Fig 4.3. It shows that the area enclosed by the curve and two axis is very large. This is a consequence of the genuine-imposter distribution as the FMR-FNMR curve is determined using the match scores.
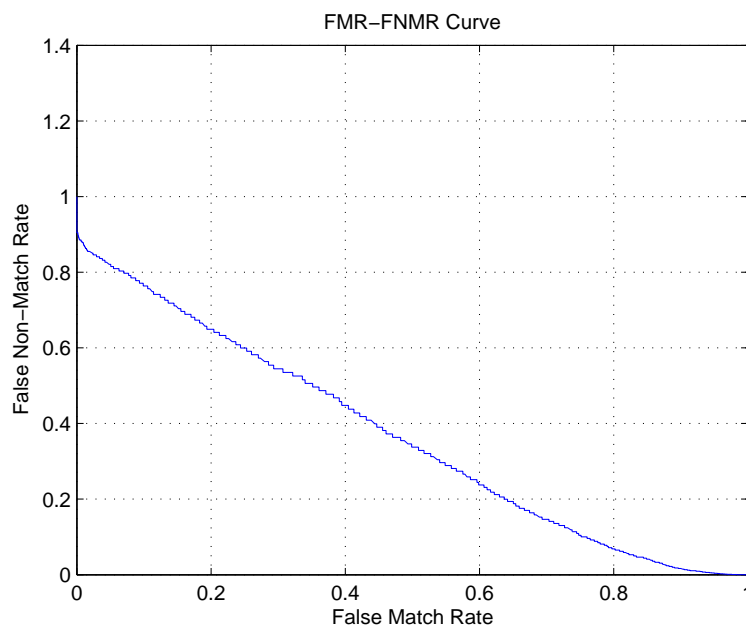
Figure 4.3: The FMR-FNMR curve for the classification of the covariance features with the modified FDA.

4.5   Discussion

The covariance features and the Fisher discriminant classifier fail to accurately identify the iris templates. The modified Fisher discriminant uses the regularized singular value decomposition because of the difficulty in calculating the inverse covariance matrix during the mapping process. Moreover, the Fisher feature space is changed due to the presence of noise, which distorts the classifying hyperplane between the feature classes.

4.5.1 Inverse Covariance Matrix

The variance of a random variable describes the extent of dispersion of all elements from the expected value, usually the mean. Define a random variable X, and the mean of X is given as $\mu = E(X)$. Then, the variance is given as:

$$Var(X) = E((X - \mu)^2) \tag{4.13}$$

The covariance extends the concept of variance to a higher dimension. For a random variable vector $X = \begin{bmatrix} x_1 \\ ... \\ x_n \end{bmatrix}$, the covariance between vector i and j could be formulated as:

$$Cov(i, j) = E[(X_i - \mu_i)(X_j - \mu_j)] \tag{4.14}$$

in which μ_i and μ_j represent the mean of X_i and X_j respectively.

The covariance matrix is the collection of all possible covariance entries, with each element in the matrix Σ_{ij} defined as the covariance between vector i and j:

$$\begin{bmatrix} cov(1,1) & ... & cov(1,n) \\ & ... & \\ cov(n,1) & ... & cov(n,n) \end{bmatrix} \tag{4.15}$$

In the definition of the Fisher discriminant, the within-class covariance matrix S_W is constructed from all feature vectors, symmetrical along the first diagonal. For the feature vectors applied in this thesis, they are vectors of dimension 400, therefore the S_W is a matrix of 400 by 400 in size. Creating the Fisher mapping matrix involves the inversion of the covariance matrix, which is most likely to be ill-conditioned in this large dimension. It is difficult to effectively calculate the inverse covariance matrix of S_W, and this is one of the reasons that the Fisher discriminant analysis fails to classify the iris feature templates in our experiments.

4.5.2 SVD and Feature Space Modeling

The covariance matrix S_W of size m-by-m could be factorized into a product of three matrices using singular value decomposition:

$$S_W = USV^T \tag{4.16}$$

in which U is an m-by-m unitary matrix that $UU^* = I_m$ or $U^{-1} = U^*$, S is an m-by-m diagonal matrix with non-negative values only on the main diagonal, and V is an m-by-m unitary matrix that $VV^* = I_m$ or $V^{-1} = V^*$.

We model each class of the feature vectors (iris feature templates) as a cluster of feature points in the feature space or the Fisher classification space. In Fig 4.4, two classes of the iris feature templates are modeled as two ellipses. The singular value decomposition generates the principal components of the data sets as PC1 and PC2. The PC1 corresponds to the largest eigenvalue, and the most representative feature vector. In the case of the Fisher discriminant analysis, the PC2 direction is used to find a hyperplane that could maximize the distance between two data-sets.

As shown in Fig 4.4, a line $\overline{AB}$ is drawn between PC1 and PC2. This line $\overline{AB}$ represents a hyperplane, and all data-sets from both classes are mapped perpendicularly onto this hyperplane. Then, the classification distance is calculated between these mapped points along the hyperplane $\overline{AB}$. According to the linear discrimination analysis, this distance has the maximum capability to linearly distinguish the two classes, and the classification hyperplane $\overline{AB}$ is between the two PC2 from both data-sets. Any new feature template to be identified is compared to each class, and the closest one is used as an indication of a correct match.
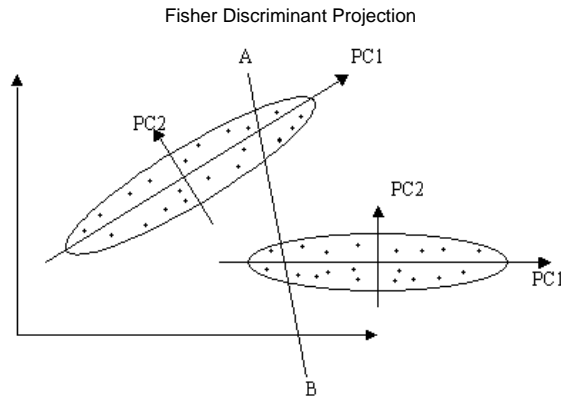

Figure 4.4: Fisher discriminant projection. The classification hyperplane is along the direction of AB, between the PC2 directions from both classes.

However, during the calculation of the within-class covariance matrix S_W and the subsequent mapping, any noise data would have a minor influence on the PC1 direction,

but a major impact on the PC2 direction. The erroneous PC2 components result in a incorrect projection direction of $\overline{AB}$, which finally results in the failed iris recognition.
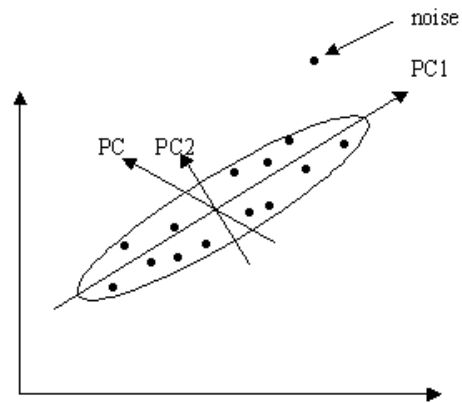

Figure 4.5: Modeling of the Fisher feature space. Feature points from the same class are modeled within one ellipse. The existence of noise distorted the PC1 direction slightly, but this noise distorted the PC2 direction completely.

Chapter 5

Fourier Feature

5.1 Introduction

One problem with the iris recognition system is the compensation for the geometric degrees of freedom: shifting, scaling and rotating [43]. The shifting comes mainly from the movement of the eyes in the plane which is orthogonal to the camera's optical axis. During the image acquisition, a person moving or tilting the face around the camera's optical axis could result in the rotational offsets of the iris images.

In chapter 1, various compensation techniques are explained. In particular, the Daugman system compensates the shifting and the scaling by unwrapping a circular iris image into a normalized polar scale template. As for the rotational compensation, it is resolved with a comprehensive search: the shifting of the iris template in the polar scale which corresponds to the rotation in the Cartesian scale.

For the Wildes system, the scaling and the rotation are compensated during the image registration, by minimizing the energy difference defined in Equation 5.1 [13]:

$$\int_x \int_y (I_d(x,y) - I_a(x-u, y-v))^2 dx dy \tag{5.1}$$

between the mapped image and the comparison image according to the mapping function:

$$\begin{pmatrix} x' \\ y' \end{pmatrix} = \begin{pmatrix} x \\ y \end{pmatrix} - sR(\phi) \begin{pmatrix} x \\ y \end{pmatrix} \tag{5.2}$$

The above two methods of the rotation compensation take place either in the image representation or in the pattern matching stage. In this chapter, the feature extraction is achieved by applying the Fourier transform to the unwrapped iris image templates in the

normalized polar scale, and using the magnitude information as the rotational-invariant features. The pattern matching is examined with the weighted Euclidean distance, and the performance evaluation is illustrated.

5.2   Localization and Unwrapping

The preprocessing of an iris image includes localizing the iris boundary, the pupil boundary, the upper and lower eyelids. In fact, the eyelash detection techniques developed and discussed in chapter 2 are applied into this preprocessing as well. After the iris regions of the image are separated from the rest, they are unwrapped according to the Daugman's rubber sheet model into iris template representations in the normalized polar scale before the subsequent feature extraction and pattern matching procedures.

These two steps of preprocessing are briefly stated here, and the detailed description could be found in chapter 2.

5.2.1   Localization

The localization of the iris region, including the iris boundaries and pupil boundaries, is accomplished using the standard circular detection technique: the edge detection and the Hough transform.

The Sobel edge detector is used to perform the two dimensional convolution with a 3×3 kernel to recover the absolute spatial gradients which correspond to the edges. Two typical convolution kernels are used in the Sobel detection, including the vertical edge detector G_x:

$$G_x = \begin{bmatrix} -1 & 0 & 1 \\ -2 & 0 & 2 \\ -1 & 0 & 1 \end{bmatrix} \tag{5.3}$$

and the horizontal edge detector G_y:

$$G_y = \begin{bmatrix} 1 & 2 & 1 \\ 0 & 0 & 0 \\ -1 & -2 & -1 \end{bmatrix} \tag{5.4}$$

These two masks respond to the vertical edge and horizontal edge respectively, and their combined absolute magnitude G is used to indicate the pixels along the edges:

$$|G| = \sqrt{G_x^2 + G_y^2} \tag{5.5}$$

Another computation efficient way of calculating G is:

$$|G| = |G_x| + |G_y| \tag{5.6}$$

Even though the orientation of the edge could be calculated by the relativity of G_x and G_y, it is normally used only with the magnitudes.

After the Sobel edge detection, the Hough transform is applied to the binary edge map to locate possible circles. Different circular parameters, (r, x_0, y_0), are polled through the binary edge map to find out the circular contour with the most amount of edge points.

$$(x - x_0)^2 + (y - y_0)^2 = r^2 \tag{5.7}$$

5.2.2 Noise Elimination

The unwanted artifacts, like the eyelash occlusion, the eyelid occlusion and the specular reflections, affect the performance of the feature extraction and the pattern classification. Using the same method as in Chapter 2, the artifact pixels are located. One of the tested iris images is shown in Fig 5.1. After the segmentation and the eyelash detection, the resulting image to be interpolated and sampled is shown in Fig 5.2.
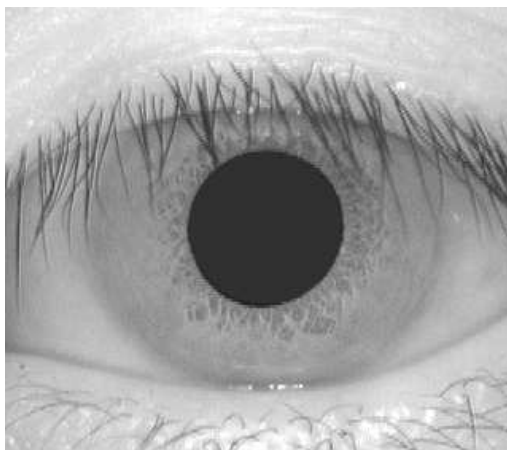

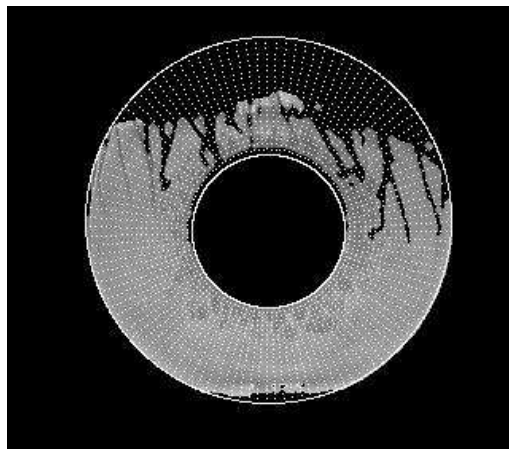Figure 5.1: The original iris image selected from the CASIA database

Figure 5.2: Segmented iris image. The original iris image is segmented within the iris and the pupil circular boundaries. The eyelashes are detected and eliminated from the pattern comparisons.

Before the next step of unwrapping into the normalized polar scale, the noise pixels have to be interpolated or estimated from the adjacent pixel intensities. An averaging filter F is applied to the image in order to estimate the noise region:

$$F = 1/25 \begin{bmatrix} 1 & 1 & 1 & 1 & 1 \\ 1 & 1 & 1 & 1 & 1 \\ 1 & 1 & 1 & 1 & 1 \\ 1 & 1 & 1 & 1 & 1 \\ 1 & 1 & 1 & 1 & 1 \end{bmatrix}$$

The interpolation only applies to the identified noise region, meaning that the rest of valid iris image information is retained for subsequent processing, as shown in Fig 5.3.

5.2.3   Representation

The Daugman rubber sheet model is adopted for the image representation, unwrapping and mapping the image pixels from the Cartesian scale to the normalized polar scale according to Equations 2.8 and 2.9.

In our test, 20×20 sampled feature pixels are used to generate the rectangular iris
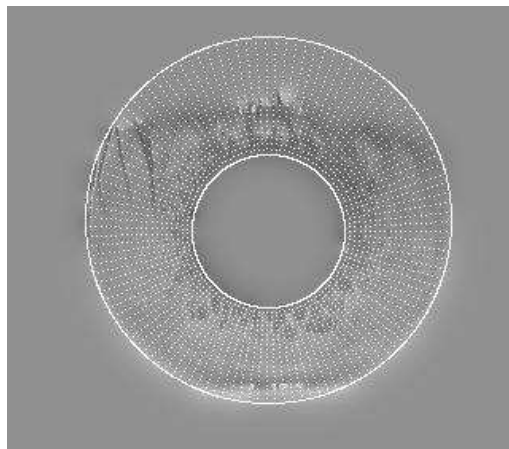
Figure 5.3: The interpolation over the identified noise pixels. The pixel intensities within the identified noise region are interpolated with a 5 by 5 averaging filter, and the pixel intensities within the valid iris region are kept as original .

templates. The same iris image in Fig 5.1 is represented in the polar scale as Fig 5.4. This is the gray-scale image template that is applied for the Fourier feature extraction, before the comparison and identification.

5.3 Fourier Feature Extraction

The Fourier transform decomposes a continuous signal into a sum of its spectrum components in the frequency domain. Like a prism splits the visible light into a spectrum of colors with different frequencies, the Fourier transform maps the signal into a series of magnitudes and phases for various frequency components. The Fourier transform $F(\omega)$ of a continuous signal $f(t)$ is defined as:

$$F(\omega) = \frac{1}{\sqrt{2\pi}} \int_{-\infty}^{+\infty} f(t)e^{-i\varpi t}dt \tag{5.8}$$

The discrete Fourier transform (DFT) is derived from the Fourier transform to analyze a discrete signal in its corresponding time-frequency or spatial-frequency domain. In the case of iris recognition, the digital images of iris texture patterns are analyzed with DFT

Figure 5.4: An iris image in the normalized polar scale. The segmented iris image is unwrapped into this rectangular iris template according to the Daugman rubber sheet model.

to extract the Fourier features from the gray-scale intensity values. In a wide variety of cases, the fast fourier transform (FFT) is used to increase the computation efficiency.

A series of N discrete signals $x_0, x_1, ..., x_{N-1}$ is transformed into a series of N complex Fourier coefficients $X_0, X_1, ..., X_{N-1}$ according to:

$$X_k = \sum_{n=0}^{N-1} x_n e^{-\frac{2\pi i}{N}kn} \tag{5.9}$$

in which $k = 0, 1, ..., N - 1$ is the index of the Fourier coefficients.

In the same way, the inverse discrete Fourier transform (IDFT) is defined as:

$$x_n = \frac{1}{N} \sum_{n=0}^{N-1} X_k e^{-\frac{2\pi i}{N}kn} \tag{5.10}$$

The DFT coefficients $X_0, X_1, ..., X_{N-1}$ represent the amplitudes and phases of different sinusoidal components from the input signal. DFT has many useful properties that give itself a wide range of applications. In this chapter, we utilize the property of the circular shift invariance in the coefficient magnitudes to achieve the rotational invariant feature extraction. Specifically, for discrete signal $x_0, x_1, ..., x_{N-1}$, the magnitudes of the DFT coefficients $|X_0|, |X_1|, ..., |X_{N-1}|$ are the same as the DFT coefficients of the circularly shifted signal $x_{N-1}, x_0, x_1..., x_{N-2}$, and vice versa.

From the previous unwrapping process according to Equation 2.8 and Equation 2.9, the segmented and interpolated iris image in Fig 5.3 is mapped into the normalized polar scale as in Fig 5.4. As a result, the rotational offset in Fig 5.3 is equivalent to the circular shift offset along the row-wise direction in Fig 5.4. DFT is applied to the unwrapped iris template in Fig 5.4. The magnitudes of the complex DFT coefficients are combined into one feature vector. This feature vector would be circular shift invariant in Fig 5.4, while it accomplishes rotational invariance in the image as shown in Fig 5.3.

During the implementation, the DFT of the unwrapped iris template could be done in two ways:

- Applying the 2-D FFT to the whole iris template and taking the magnitude of each coefficient as shown in Fig 5.5.

Figure 5.5: Fourier magnitude matrix after 2-D FFT. 2-D FFT is applied to the unwrapped iris image intensity matrix. The magnitude matrix is computed from the complex FFT coefficient matrix.

- Applying the 1-D FFT to the iris template row by row, and taking the magnitude information, which is shown in Fig 5.6.

The latter one using 1-D FFT would extract the feature only along the row-wise direction, which corresponds to the concentric ring in iris images. Both of them would have the same rotational-invariant feature, and both systems are evaluated below.
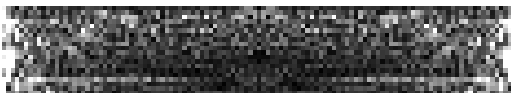
Figure 5.6: The Fourier magnitudes matrix after 1-D FFT. FFT is applied to the unwrapped iris image intensity matrix row by row.

5.4 Classification with Weighted Euclidean Distance

With the extracted feature templates as shown in Fig 5.5 and Fig 5.6, different iris templates are compared to each other in terms of the weighted Euclidean distance. In this thesis, only an averaged Euclidean distance is used, with no specific weights on any frequency components. For iris identification, each iris feature template is compared to all other iris feature templates in the database.

5.5 Performance Evaluation and Discussion

The performance is evaluated with the same database used in Chapter 2 and Chapter 3, including 327 selected low quality iris images with partial eyelash occlusions. The classification based on the WED between templates is evaluated, and several evaluation metrics are plotted for analysis, like the cumulative match curves, the detection error rate curves and the genuine-imposter distributions.

5.5.1 Fourier Feature with 2-D FFT Magnitudes

With 2-D FFT magnitude feature matrix as described above, the genuine-imposter distributions are plotted in Fig 5.7. The solid line represents the histogram of the genuine distances within the same class (images taken of the same eye), and the dotted line represents the histogram of the imposter distances between different classes (different eyes). It is shown that the Fourier feature manages to distinguish the iris feature templates from each other. The feature templates based on the Fourier transform magnitudes extract the frequency components within the image intensity vectors, but these features do not equal the performance of the features extracted with the Gabor wavelet decomposition.
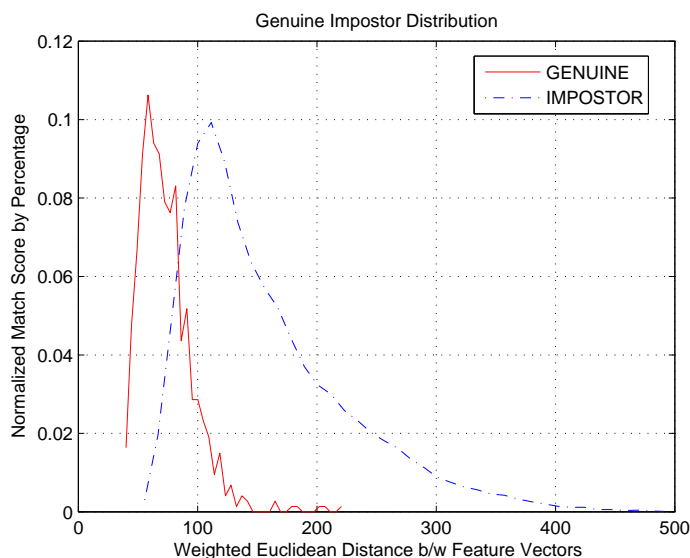

Figure 5.7: The genuine imposter distributions of the 2-D Fourier feature extraction. The magnitude matrices after the 2-D Fourier transform are used as the feature templates for classification.

The cumulative match curve of the 2-D Fourier features is shown in Fig 5.8. The rank-1 identification rate is 77.68%, and it achieves the rotational invariance at the same time.

The DET curve is shown in Fig 5.9. It shows that the false non match rate drops sharply with the increase of false match rate.
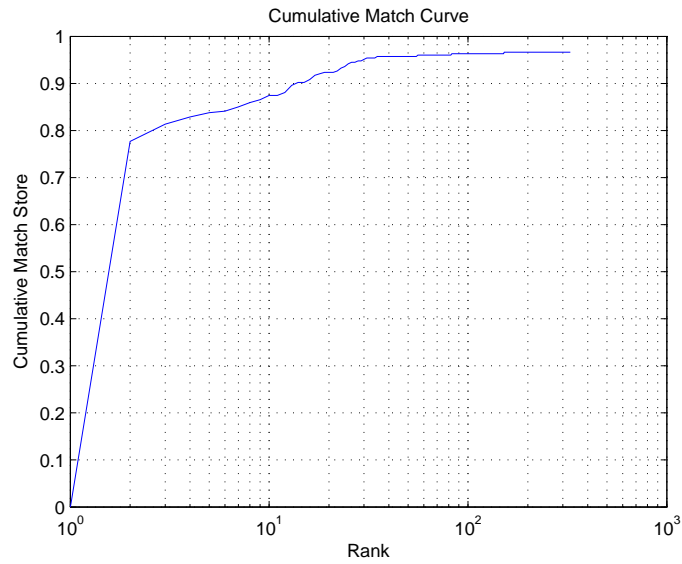
Figure 5.8: Cumulative match curve of the 2-D Fourier features. It is shown that a rank-1 identification rate of 77.68% is achieved.
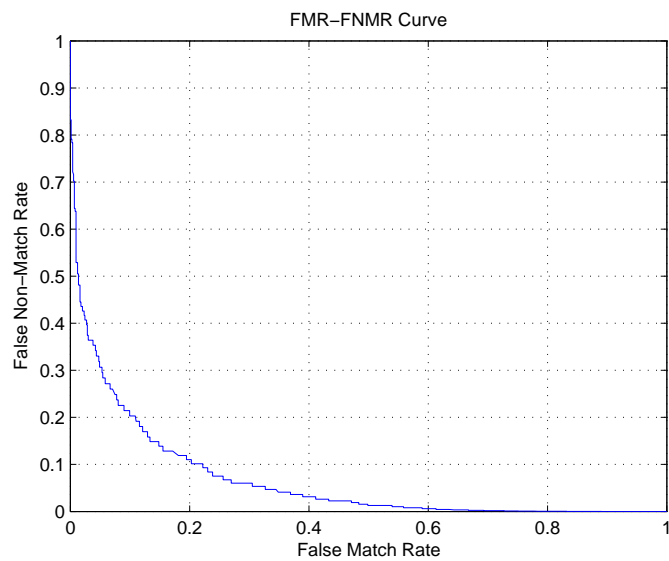

Figure 5.9: DET curve of the classification with the magnitude feature templates from the 2-D Fourier transform.

5.5.2 Fourier Feature with 1-D FFT Magnitudes

The 1-D FFT magnitude rotational invariant features demonstrate a comparable performance to the 2-D FFT magnitude rotational invariant features. It achieves a rank-1 identification rate of 78.28%, and a similar CMC curve in Fig 5.11 and the DET curve in Fig 5.12. With the 1-D FFT feature, the genuine-imposter distributions in Fig 5.10 is compared to the genuine imposter distributions in Fig 5.7. we could see that both the genuine and imposter distances are significantly higher in 2-D Fourier features than in 1-D Fourier features, even though their relative distributions remain similar.
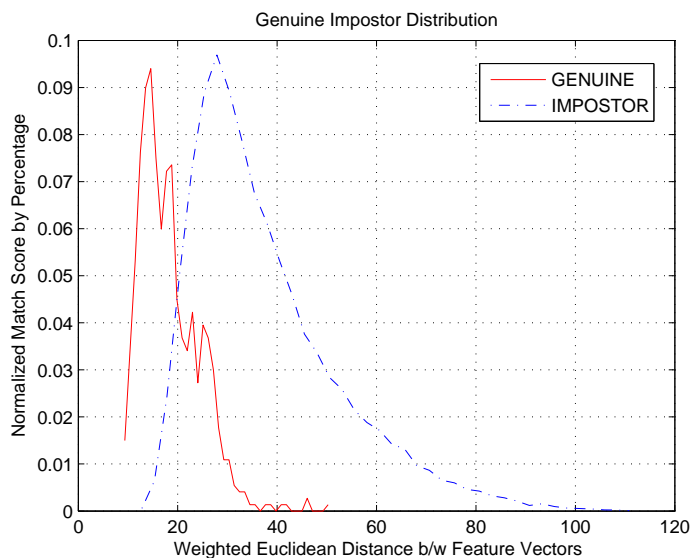

Figure 5.10: Genuine imposter distribution of the 1-D Fourier features. 1D Fourier magnitude matrices are used as the feature templates.

5.6 Discussion

Iris recognition relies on the abundant feature information embedded in the texture patterns, which are better represented in the frequency domain than in the spatial domain. The Fourier transform is able to decompose the iris texture information into the frequency domain, and illustrate this information in terms of the magnitude of different sinusoidal components. From the above performance evaluation, we have seen that the algorithm based on the Fourier features could determine unique features for identification purpose and accomplish an identification rate around 77%.
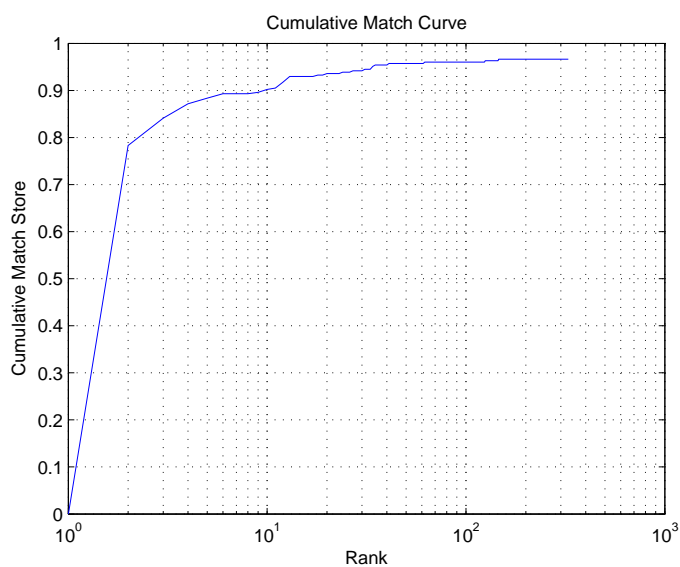
Figure 5.11: Cumulative match curve of the 1-D Fourier feature. In this case, a Rank-1 identification rate of 78.28% is observed.
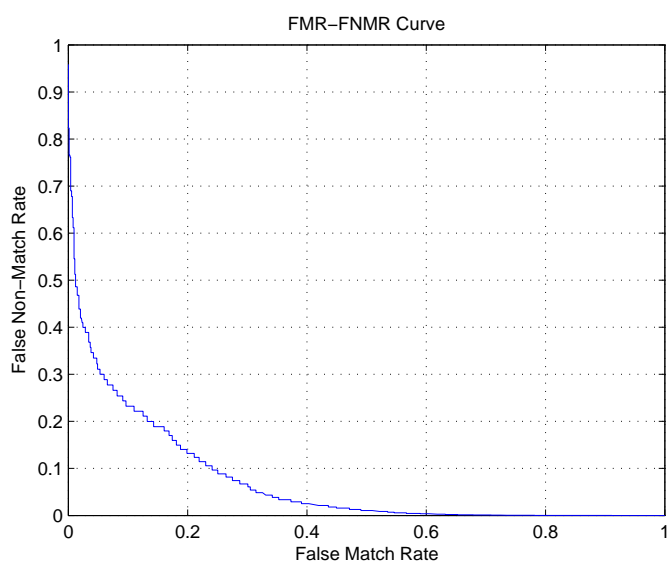

Figure 5.12: FMR-FNMR curve of the classification with the feature templates from the 1-D Fourier transform.

On the other hand, this Fourier transform based iris recognition algorithm does not match the performance of either the Gabor or the Log-Gabor wavelet based feature extractions, because of the loss of phase information within local texture patterns.

The wavelet transform analyzes the signal with various wavelet functions that are dilated and translated from a mother function, such as the Haar wavelet and the Gabor wavelet. It is localized in the spatial and frequency domains, which give more insights into the local features of the signal. Such image processing techniques with the Gabor wavelets have been utilized in many applications, such as the contrast enhancement in MRI images [44] and the texture segmentation [45]. The Gabor filter bank could be seen as a sinusoidal plane of particular frequency and orientation, modulated by a Gaussian envelope [46]:

$$h(x,y) = exp[-\frac{1}{2}(\frac{x^2}{\sigma_x^2} + \frac{y^2}{\sigma_y^2})]cos(2\pi\mu_0 x + \phi) \qquad (5.11)$$

in which σ_x and σ_y represent the standard deviation of the Gaussian envelope, μ_0 and ϕ represent the frequency and phase of the sinusoidal wavelets, θ represents the orientation of the Gabor filter.

Within the Gaussian window centered around various regions of the iris image, the Gabor wavelet maps the texture information into the sinusoidal analyzing functions with different frequencies, phases and orientations. The most important features in an iris image are within the local texture patterns, since the intensity values that are far apart tend to have less correlation. Therefore, this particular window and analyzing functions are well suited to extract the iris local features, and the Daugman algorithm [7] based on the Gabor filter banks have been the most successful and widely-used iris recognition algorithm.

On the other hand, the Fourier transform extracts the frequency components from the entire image intensity vectors, as compared to the Gabor wavelet transform which extracts the frequency information from local regions. In addition, a significant portion of the information is contained in the phase content of the image texture pattern. The Fourier magnitude features lose the phase information. Therefore the Fourier magnitude based feature extraction fails to perform as well as the Gabor feature extraction.

Overall, the comparison between the Fourier transform and the discrete Wavelet transform shows that most of the unique iris features are within the local regions of iris patterns. To make the maximum use of this information, it is best to utilize a localized feature extractor with a suitable analyzing function.

Chapter 6

Progressive Segmentation and Feature Analysis

6.1 Introduction

In the previous chapters, various issues regarding iris recognition have been examined and discussed, like the enhanced segmentation, the artifact elimination and the rotational invariant feature extraction. These approaches aim to improve the system robustness and performance, and to utilize the maximum amount of the statistical variability within the iris texture patterns.

One general assumption behind the enhanced segmentation and noise-removal approaches is that more accurate iris image information results in better identification performance. Therefore the eyelash detection is able to explore more valid iris pixels while eliminating the invalid eyelash pixels; the improved circular detection tries to localize more accurate iris and pupil boundaries; the rotational invariant feature extraction compensates the offsets from the camera tilting and the image shifting during the acquisition period.

There is another question to be answered: what is the quantitative relationship between the quantity of iris image information and the recognition system performance?

In this chapter, we investigate the above concept in terms of the image feature points sampling resolution and the band-limited image segmentation.

6.2 Method Description

The method here is to take a limited amount of iris pixels for the iris recognition algorithm, and evaluate the performance metrics.

Two ways are used to take the limited amount of iris pixels: a limited image area and a limited pixel sampling resolution. And the recognition algorithm applied here is the Daugman rubber sheet model [7], the Log-Gabor feature extraction [22] and the Hamming distance for decision making.

6.2.1 Progressive Segmentation

The circular boundaries of iris and pupil regions are localized with the standard Hough transform. Then, an area of a given width is selected from the original iris image for the feature extraction, as is shown in Fig 6.1. Two parallel lines on both sides of the pupil center are drawn across the iris image. The distance between these parallel lines is called the bandwidth, in unit of pixels. Then the iris region surrounded by the iris circle, the pupil circle and the two parallel lines is chosen for the subsequent feature extraction.

Iris regions, within the pupil and iris boundaries but outside the two parallel lines, are masked out, which are shown by the shaded area in Fig 6.1.

Because of the subsequent Gabor filtering, these masked out iris regions will be given a certain value for the convolution purpose. In this case, the average intensity value of all the non-masked iris region is used to fill into these masked iris regions. However, during the process of decision making, the Hamming distance is calculated using only between the selected iris regions from two iris images. Basically, we compare the features from those selected iris regions to determine if the iris image information is enough for the recognition application.

6.2.2 Progressive Feature Points Sampling

Other than the band selection, various resolutions of intensity pixels could be selected for the subsequent unwrapping and the Gabor filtering.

The feature points are sampled along the radial and circumferential directions. A sampling line runs across the iris region between the iris boundary and pupil boundaries. And a fixed number of gray-scale intensity pixels are sampled along the line.

At the same time, the sampling line rotates around the pupil center for a specific angle, and another set of feature points are sampled. Therefore, two parameters are used
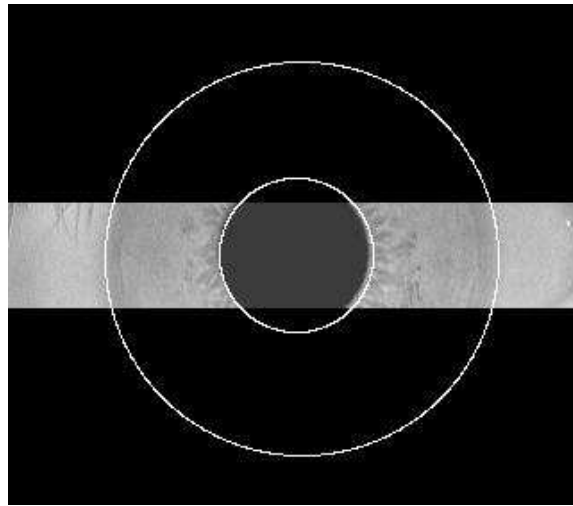
Band−limited Segmentation

Figure 6.1: The segmentation with a bandwidth of 60 pixels. Within the segmented iris region, an area is selected with a bandwidth of 60 pixels. And the rest of the iris region is discarded from the feature extraction and the pattern matching.

to simulate the sampling resolution: the radial resolution, which specifies the amount of points on the sampling line and the circumferential resolution, which specifies the amount of sampling lines over the 360°.

A collection of intensity feature points are sampled from the iris image shown in Fig 6.1, with a radial resolution of 20 points and a circumferential resolution of 120 points. The sampling scheme is shown in Fig 6.2.
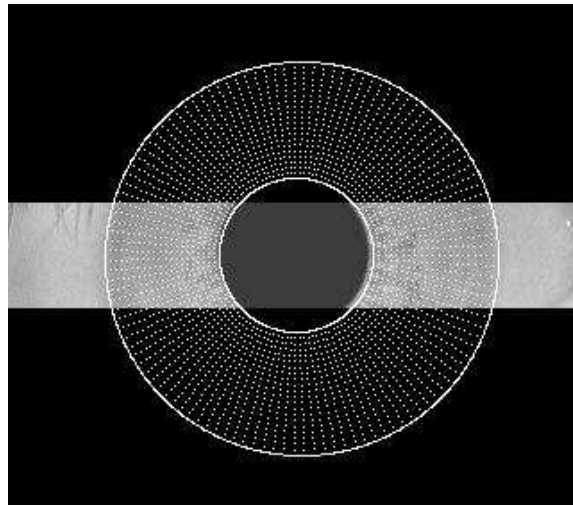

Figure 6.2: Segmentation with a sampling resolution of [20 120]. From the segmented iris region, an area of 60 pixels wide is used, and within this band-limited area, a sampling resolution of [20 120] is adopted.

6.2.3   Unwrapping and Image Representation

With the combination of the band-limited segmentation and the sampling resolution, the iris image will look like Fig 6.2 before being unwrapped into a normalized polar scale representation.

The image with all the sampled feature points, as shown in Fig 6.2, is unwrapped from the Cartesian coordinates to the normalized polar coordinates according to the Daugman rubber sheet model [7]. The mapping functions are described in Equations 2.8 and 2.9, and the unwrapped image and the corresponding mask are shown in Fig 6.3.

Unwrapped Iris Image
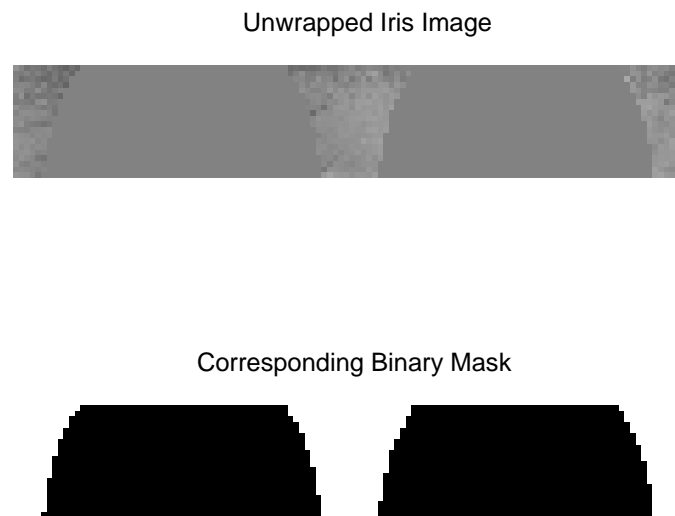

Corresponding Binary Mask

Figure 6.3: The unwrapped iris image and the corresponding mask. The band-limited segmentation of the iris image is unwrapped into the rectangular template in the top graph. The corresponding binary mask is illustrated in the bottom graph.

The unwrapped images are used for the Gabor feature extraction, and the masks are used to indicate the positions of the valid iris feature points.

6.2.4 Feature Extraction and Pattern Matching

The feature extraction is achieved by convolving the iris image matrix in Fig 6.3 with the Log-Gabor filter, and the phase information is taken as a binary feature template. The frequency response of the Log-Gabor filter is defined as in Equation 2.10.

The Hamming distance is calculated between any two iris feature templates as in Equation 1.25, among which the minimum Hamming distance indicates the correct pattern match.

6.3 Performance Evaluation

With the combination of the bandwidth limited segmentation and the progressive sampling resolution as described above, the iris feature templates are generated from a database of 327 images from CASIA [17], and compared to each other.

The evaluation metrics used here include the cumulative match curve, the genuine-imposter distribution, the detection error tradeoff curve and the rank-1 identification rate. The tested segmentation bandwidth ranges from 2 to 100 by a step of 2, and the sampling resolutions include: [10 60] (10 points along radial direction and 60 points along circumferential direction), [20 120] and [30 180].

6.3.1 Progressive Band-Limited Segmentation

In this section, the sampling resolution is fixed to 20 points on the radial direction and 120 points on the circumferential direction, while at the same time changing the bandwidth from 2 to 100. So there are 50 different combinations of these two parameters, and selected results are shown below.

Cumulative Match Curve

The cumulative match curve with a bandwidth segmentation of 40 pixels, is shown in Fig 6.4. The cumulative match score starts at a rank-1 rate of around 79%. In comparison, with a bandwidth of 80 pixels, the cumulative match curve is given in Fig 6.5, with a rank-1 rate of around 95.6% and quickly jumps to 100%.
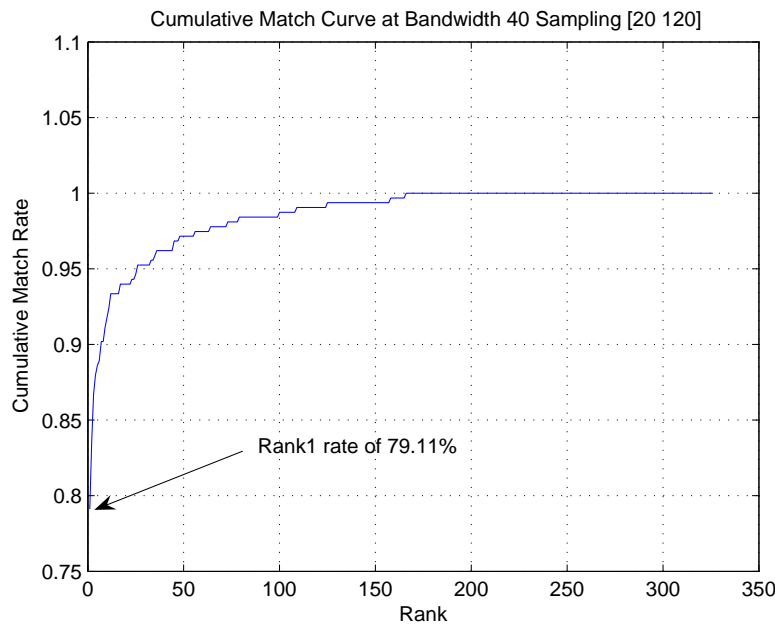
Figure 6.4: The CMC with a segmentation bandwidth of 40 pixels and a sampling resolution of [20 120]. A rank-1 identification rate of 79% is observed.

Genuine-Imposter Curve

The genuine-imposter curve illustrates how well these two distributions are separated. It is a direct indication of the algorithm's ability to classify the iris image templates. For a segmentation bandwidth of 40 pixels, the genuine-imposter curve is shown in Fig 6.6, in which the solid line represents the genuine distribution, and the dotted line represents the imposter distribution. As a comparison, Fig 6.7 shows the genuine-imposter curve for a selected image bandwidth of 80 pixels.

The two distributions in Fig 6.6 have a large amount of overlap, and their respective peaks are not as high as the two distributions in Fig 6.7. This indicates a higher classification capability as a result of a higher bandwidth.

Rank-1 Rate Curve

The rank-1 rate curve combines all the rank-1 identification rate from all 50 cases of bandwidth selections with the same sampling resolution, and plots into one graph, as shown in Fig 6.8. It shows how quantitatively and gradually the rank-1 identification rate increases with the broadening of the bandwidth.
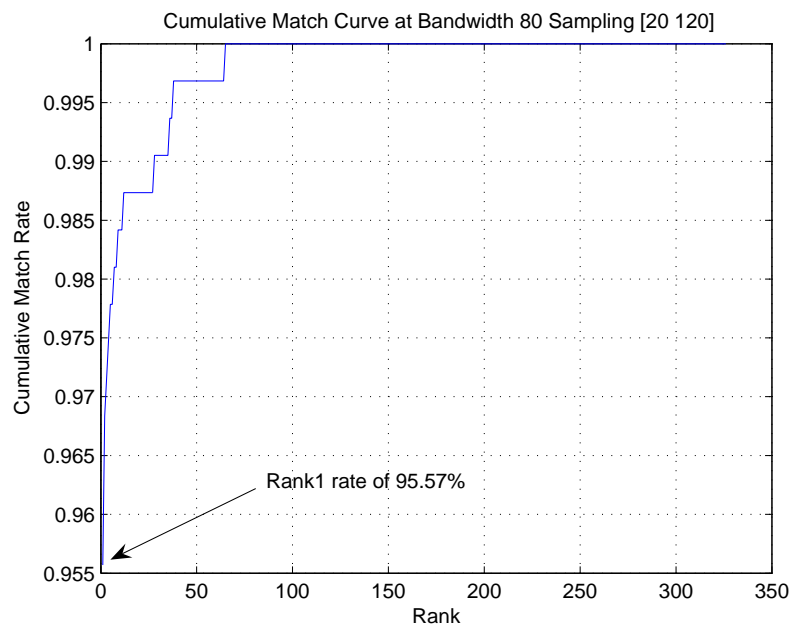
Figure 6.5: CMC with a segmentation bandwidth of 80 pixels and a sampling resolution of [20 120]. A rank-1 identification rate of 95.6% is observed, which is significantly higher than the rank-1 rate from bandwidth of 40 pixels.
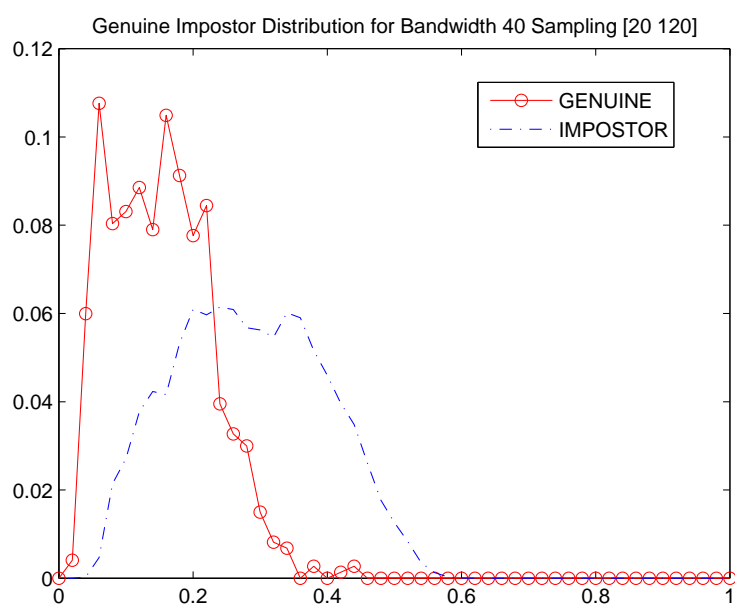
Figure 6.6: The genuine imposter curve with a segmentation bandwidth of 40 pixels and a sampling resolution of [20 120]. It is observed that there is still a large portion of overlapping between the genuine and imposter distributions.
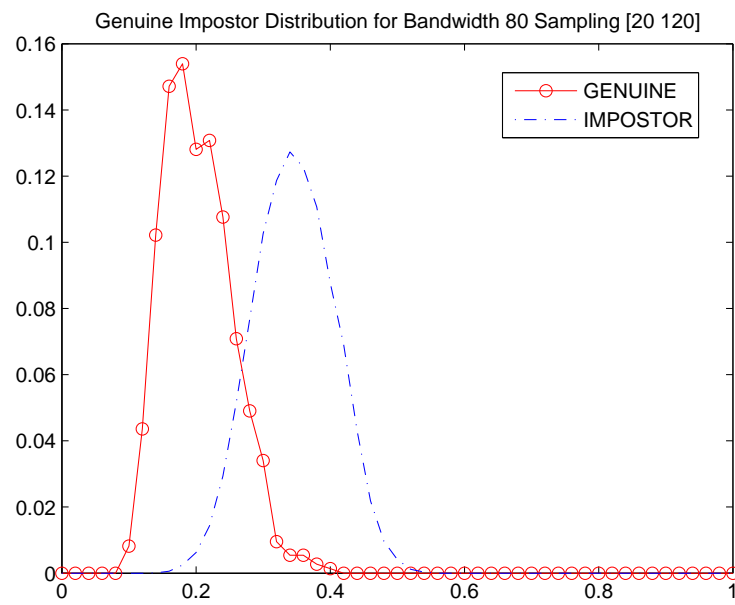
Figure 6.7: The genuine imposter curve with a bandwidth of 80 pixels and a sampling resolution of [20 120]. The overlapping region between the genuine and imposter distributions is significantly reduced, as compared to Fig 6.6.

With a sampling resolution of 20 feature points along the radial direction and 120 feature points along the circumferential direction, the rank-1 rate increases rapidly to 95.6% within a bandwidth range of 10 and 30 pixels. After that, the performance stops to improve and even fluctuates up and down. First of all, with a widening bandwidth, the selected iris region starts to include the regions with certain eyelash and eyelid occlusions, which contribute the performance fluctuation. Second, the amount of image information has reached the saturation level for the algorithm.
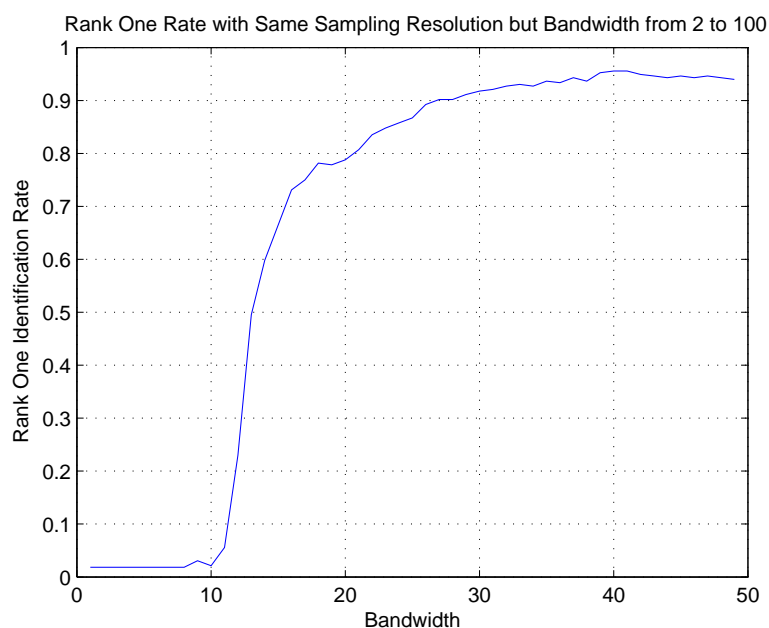
Figure 6.8: The rank-1 rate with the bandwidths from 2 to 100 and a sampling resolution of [20 120].

FMR-FNMR Curve

The FMR-FNMR curves from several different bandwidths are plotted in one graph for comparison, as illustrated in Fig 6.9. Four curves, named as DET1 DET2 DET3 DET4, represent the bandwidth of 20, 40, 60 and 80 pixels respectively. The improvement is dramatic, and there is hardly any room for further improvement after a certain bandwidth.
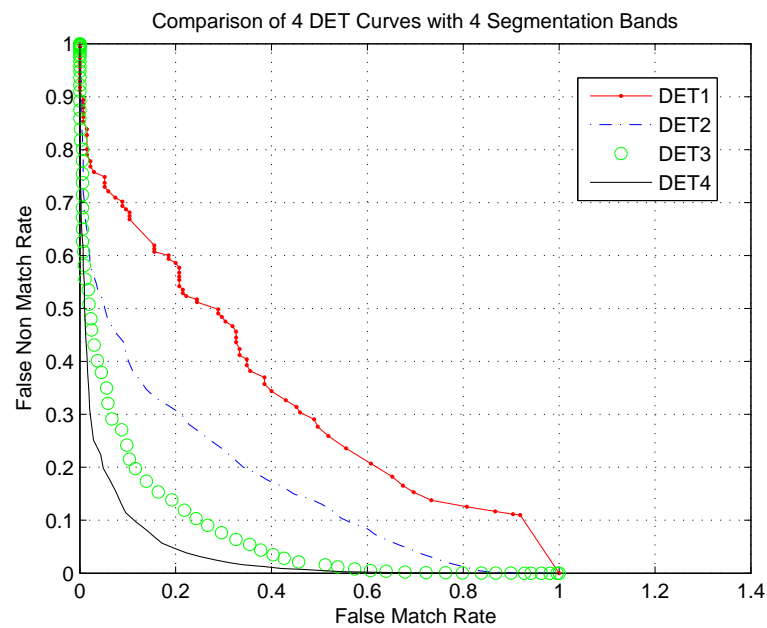
Figure 6.9: DET curve comparison between different bandwidths. The four curves, red, blue, green and black, represent the bandwidth of 20, 40, 60 and 80 pixels respectively. The DET performance improves with the increase of bandwidth.

6.3.2 Progressive Sampling Resolution

In this section, the sampling resolution is kept the same while changing the band-limited segmentation of the iris images for the feature extraction and the pattern recognition. Generally, it shows similar performance in the cumulative match curve, the genuine imposter distributions, the rank-1 rate curve and the detection error trade-off curve.

The iris identification accuracy increases with the increase in the sampling resolution when the segmentation band is fixed. It also experiences a similar critical range after the performance stops to increase and fluctuate.

Cumulative Match Curve

The cumulative catch curves from two different sampling resolutions but the same bandwidth segmentation are compared to illustrate the performance difference when a higher feature point sampling resolution is applied. In Fig 6.10, it is observed that with 20 feature points along the radial direction and 120 feature points along the circumferential direction, it achieves a rank-1 identification rate of 92.09%. In comparison, when sampling 30 feature points along the radial direction and 180 feature points along the circumferential direction, a rank-1 identification rate of over 98.73% is achieved.
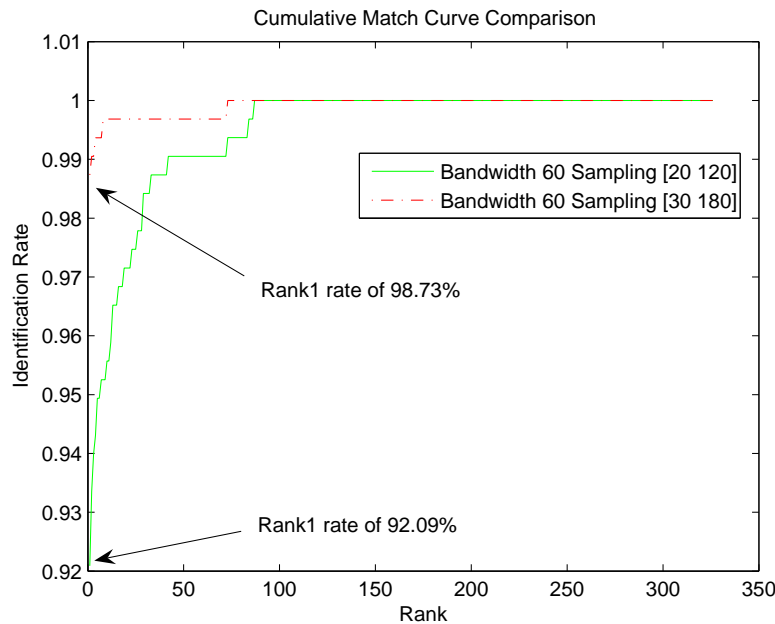

Figure 6.10: CMC comparison of the sampling resolutions of [20 120] and [30 180].

Genuine-Imposter Curve

The genuine-imposter distributions with the above sampling configurations of [20 120] and [30 180] are calculated and compared to each other, as shown in Fig 6.11.

The upper graph shows the genuine imposter distribution when 20 feature points are sampled along the radial direction and 120 feature points are sampled along the circumferential direction. The lower graph shows the genuine imposter distribution when 30 feature points are sampled along the radial direction and 180 feature points are sampled along the circumferential direction.

The separation of the genuine and imposter histograms is largely improved because of the increased sampling resolution. The separation of the two peaks indicates the classification capability of the two systems. Clearly, with a higher sampling resolution, more feature points are selected in the rectangular representation of the iris patterns, and the separation among the genuine and imposter distributions is improved.
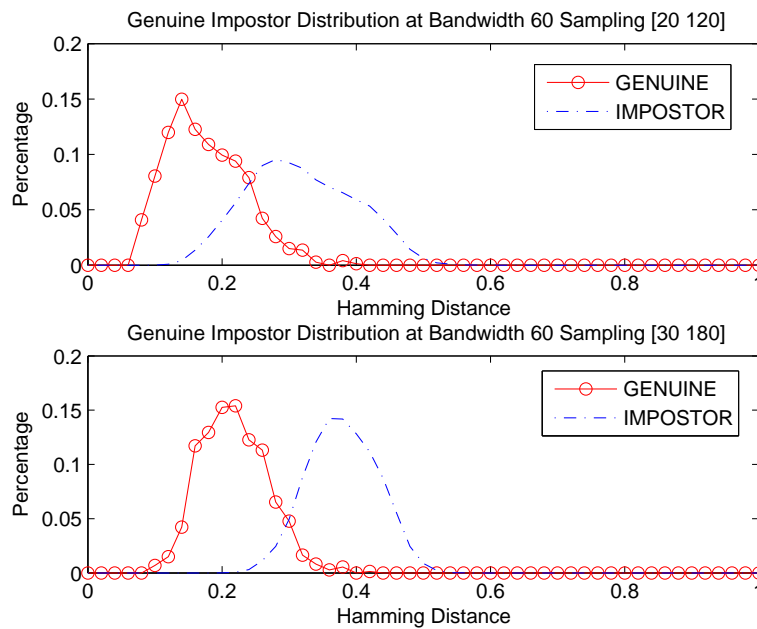

Figure 6.11: The genuine imposter distribution comparison of two different sampling resolutions: [20 120] and [30 180].

Rank-1 Identification Rate

The rank-1 identification rate curve combines the rank-1 rate from the gradually increased sampling resolutions with a fixed bandwidth. We use [20 120] to indicate a sampling scheme of 20 feature points along the radial direction and 120 feature points along the circumferential direction.

In Fig 6.12, the upper graph illustrates the rank-1 rate curve at a bandwidth of 30 but increasing sampling resolutions from [1 6] to [30 180]. We can see that the system identification rate stays almost zero until a sampling resolution of [10 60] is reached, then it quickly rises to its optimal performance of around 90%. In contrast, the lower graph in Fig 6.12 shows the rank-1 rate curve at a bandwidth of 80 with an increasing sampling resolutions from [1 6] to [30 180]. The rank-1 rate curve in the lower graph rises rapidly from a sampling resolution of [3 18], and reaches the optimal performance of close to 99%.
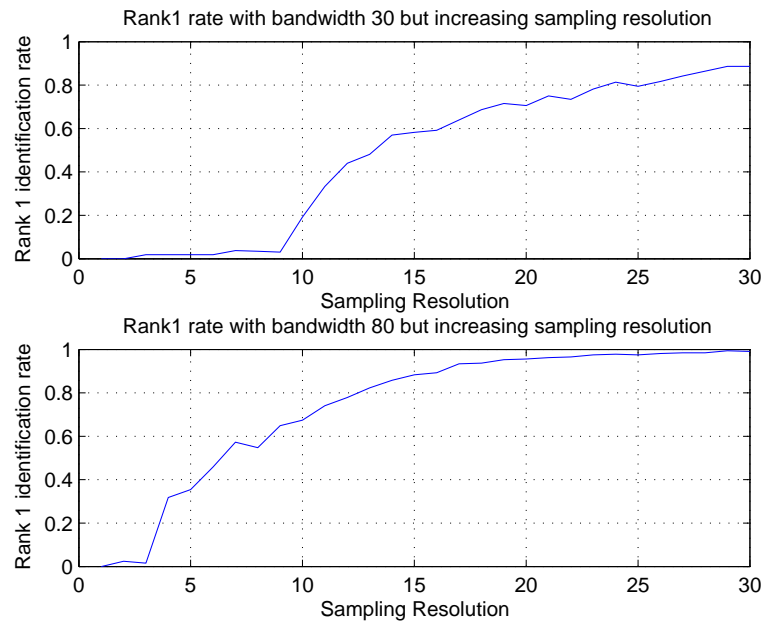

Figure 6.12: The rank-1 rate curve with increasing sampling resolutions at two different bandwidths.

FMR-FNMR Curve

In Fig 6.13, the DET curves of three different sampling resolutions are compared. The red, blue and green curves correspond to three different sampling resolutions at [10 60], [20 120] and [30 180] respectively. With an increased sampling resolution, the system performance is improved from DET1 to DET3. These different sampling resolutions with the same bandwidth are illustrated, in a sequence of [10 60], [20 120] and [30 180], in Fig 6.14, Fig 6.15 and Fig 6.16 respectively. With the same iris image, a higher sampling resolution gives a better system performance. However, the maximum sampling resolution can not exceed the limit of the camera resolution during the image acquisition. Therefore, it is an effective alternative to increase the system performance by increasing the camera resolution during the image acquisition procedure.
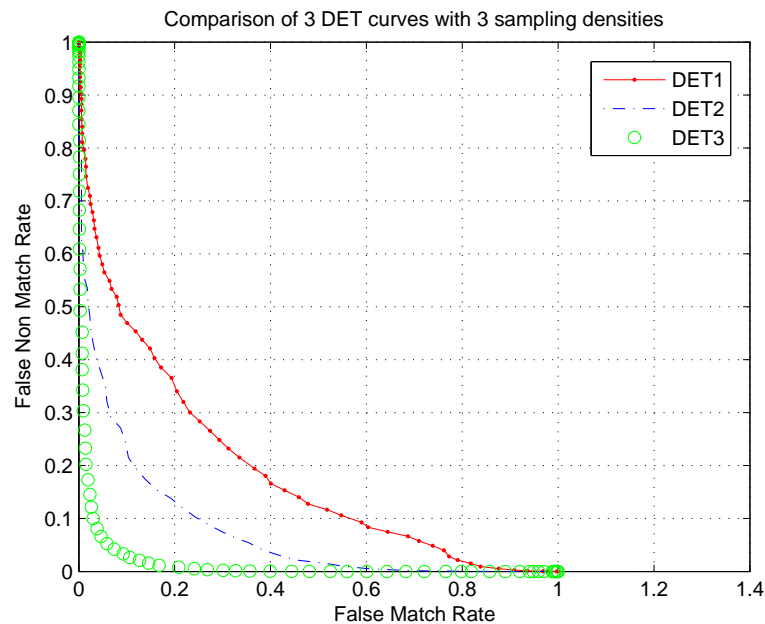
Figure 6.13: The DET comparison of three different sampling resolutions.

6.4   Discussion

The assumption of this experiment is that the system performance improves with the increase in the amount of the iris information utilized for recognition. In other words, the more valid iris image information that is applied to the system, the better will the

Bandwidth 60 pixels and Sampling density [10 60]

Figure 6.14: Segmentation with a bandwidth of 60 pixels and a sampling resolution of [10 60].

Bandwidth 60 pixels and Sampling density [20 120]
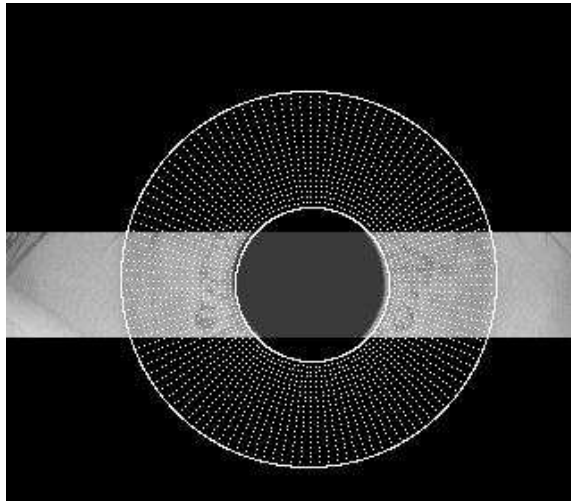
Figure 6.15: Segmentation with a bandwidth of 60 pixels and a sampling resolution of [20 120].

Bandwidth 60 pixels and Sampling density [30 180]
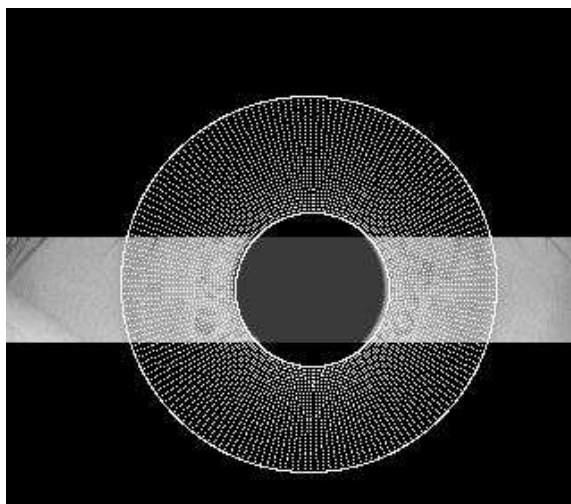
Figure 6.16: Segmentation with a bandwidth of 60 pixels and sampling resolution of [30 180].

performance be. However, the rate of performance improvement slows down after the amount of information reaches to a certain level, which we term as s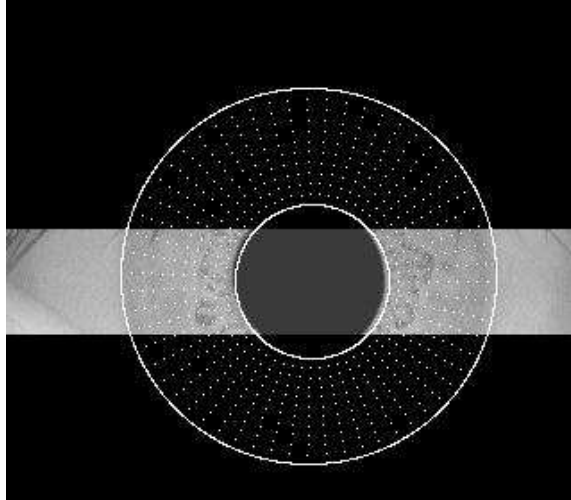aturation. This testing shows a solution for iris recognition systems that are used in difficult situations, where the image quality is low. By using more valid iris image area and sampling more feature points, the system could be improved to a satisfactory level. Therefore, it suggests an alternative to improve the performance of an iris recognition system, which is to increase the camera resolution. A higher resolution in the image acquisition implies a higher resolution of the information content used for the feature representation and the classification.

Chapter 7

Conclusion

7.1 Summary of Work

The previous comparisons and evaluations of various biometric recognition algorithms have ranked iris recognition as one of the highest in performance [47], as compared to other biometric technologies such as fingerprint recognition, hand geometry recognition, retina recognition, DNA and speaker recognition. Still, there are issues to be solved in order to further improve the accuracy and robustness of an iris recognition system. In this thesis, we have attempted to address the following issues:

- The increase of system performance with low quality iris images, particularly with eyelash occlusions.

- The effect of erroneous localizations on the system performance.

- The impact of a more accurate circular detection on the system performance.

- The introduction of a rotational invariant feature extraction scheme so that compensation is not needed during the decision making.

- The quantitative relationship between the amount of the iris image information and the identification performance.

In this thesis, all the experiments were carried out with the following assumption: more accurate iris image data result in better recognition performance.

In Chapter 2, we developed an algorithm to detect the eyelash locations, to further explore the information between the eyelashes, and to discard the distortions from the

eyelashes. The evaluation showed that this algorithm improves the error rates in DET curves except in very low FMR range. The performance improvement was marginal, but it showed an alternative for recognition with eyelash occluded iris images.

In Chapter 3, the manual edge point sampling and the circular curve fitting were used to correct the erroneous circular localizations. The system with the fixed parameters for iris and pupil boundaries were compared to the system without the circular correction. The results showed positive improvement in the following metrics: the CMC curve, the rank-1 rate and the DET curves.

Chapter 4 introduced the covariance feature extraction from the unwrapped iris image templates in the normalized polar scale. These features are rotational invariant, and they were combined with the modified Fisher discriminant analysis (FDA) for recognition. However, the performance was not satisfactory due to the existence of the random noise within the iris image classes that distorted the secondary principal component directions. Overall, we concluded that this approach failed to carry out the proper classification as shown in the genuine-imposter distributions.

In Chapter 5, the feature extraction was explored and examined using the Fourier transform magnitudes. It achieved rotational invariance and revealed the feature information in the frequency domain for the representation. This Fourier features were compared to the features with the wavelet decomposition. It showed that a significant amount of the useful iris image features were within the local iris region in the frequency domain. Therefore, the discrete wavelet transform had the advantage to extract this information as opposed to the Fourier transform that was used to extract the global frequency components. Furthermore, the Fourier magnitude-based feature extraction scheme lost the phase information. The loss of phase information was the main reason for the lower performance than the Gabor wavelet-based recognition.

Chapter 6 introduced the band-limited segmentation and the feature point sampling resolution to gradually increase the iris information and evaluate the changes in system performance. Clearly, the system performance improved with the increased iris information. And interestingly, the improvement of system performance was not uniform with the increase in iris information. Rather, it improved within a critical range, where the performance improved rapidly and reaches a saturation level. After the saturation the performance shows minor fluctuations.

7.2   Suggestions for Future Work

There are several directions to pursue for future work. First, an algorithm could be developed to enhance the circular detection, like recursive detection and verification after each circle localization. For example, the relevant positions between the iris boundaries, the pupil boundaries and the eyelid curves should be within a certain range proportional to their respective radiuses and circular center coordinates. This could be used to decide if the detected circular boundaries are accurate enough, and thus set new thresholds for the next recursive detection.

Second, the inverse covariance matrix estimation is a very important issue with the Fisher discriminant analysis, particularly when it comes to large dimensions of data vectors and the singularity issue. An effective way to calculate the inverse covariance matrix could potentially improve the system in Chapter 4. Also, it would be interesting to investigate the relative importance of the second principal component directions. And, if PCA uses the first principal component as a representative direction for the group features, it is useful to understand how much the second principal component affects the system behavior.

Another possible line of research is to use the entropy theory to analyze the information content with the progressive image segmentation. It can give further insight into how the segmentation affects the biometric entropy for recognition.

Overall, we have developed and examined various techniques that could improve iris recognition system performance with low quality iris images:

- Eyelash detection and elimination

- Improved localization of the iris and pupil boundaries

- Rotational invariant feature extractions like the Fourier features and the covariance features

- Band-limited segmentation and increased feature points sampling resolution

We have seen the potential use for these techniques in some practical applications, such as security surveillance, unsupervised capture, and iris image capture under poor lighting conditions. Some of these approaches show obvious improvement, and some other approaches indicate the weakness and importance in various aspects of the iris image feature extraction procedure. The results in this thesis help to clarify future research directions in the effort to improve the iris recognition for low quality iris images.

Bibliography

[1] A.K. Jain, A. Ross and S. Prabhakar, "An Introduction to Biometric Recognition," *Circuits and Systems for Video Technology*, vol. 14, no. 1, pp. 4–20, Jan 2004.

[2] L. O'Gorman, "An Overview of Fingerprint Verification Technologies," *Information Security Technical Report*, vol. 3, no. 1, pp. 21–32, 1998.

[3] P.J. Phillips, P.J. Flynn and K.W. Bowyer, "Overview of the Face Recognition Grand Challenge," *Computer Vision and Pattern Recognition*, vol. 1, pp. 947–954, June 2005.

[4] D. Reynolds, "An overview of automatic speaker recognition technology," *International Conference on Acoustics, Speech, and Signal Processing*, vol. 4, pp. 4072–4075, May 13-17, 2002.

[5] J. Wayman, "A Generalized Biometric Identification System Model," *IEEE Transactions on Signals Systems and Computers*, vol. 1, pp. 291–295, November 1997.

[6] F.H. Adler, *The Physiology of the Eye: clinical application*, 8th ed. edited by Robert A. Moses, St. Louis: Mosby, 1987.

[7] J. Daugman, "How Iris Recognition Works," *IEEE Transactions on Circuits and Systems for Video Technology*, vol. 14, no. 1, pp. 21–30, January 2004.

[8] J. Daugman and C. Downing, "Epigenetic Randomness, Complexity and Singularity of Human Iris Patterns," *Biological Sciences*, vol. 268, no. 1477, pp. 1737–1740, August 2001.

[9] J. Daugman, "Technical Report of Results from 200 Billion Iris Cross Comparisons," *University of Cambridge*, no. UCAM-CL-TR-635, June 2005.

[10] E.M. Newton and P.J. Phillips, "Meta-Analysis of Third-Party Evaluations of Iris Recognition," *Technical Report NISTIR 7440*, National Institute of Standards and Technology, Gaithersburg, MD, August 2007.

[11] P. Phillips, "FRVT 2006 and ICE 2006 Large-Scale Results," *Technical Report NISTIR 7408*, National Institute of Standards and Technology, Gaithersburg, MD, March 2007.

[12] Authenti-Corp, "Standards-Based Performance and User Cooperation Studies of Commercial Iris recognition Products," *Iris Recognition Study 2006 Final Report*, March 31st, 2007.

[13] R. Wildes, "Iris Recognition: an Emerging Biometric Technology," *Proceedings of the IEEE*, vol. 85, no. 9, pp. 1348–1363, September 1997.

[14] P. Kronfeld, "The Gross Anatomy and Embryology of the Eye," *The Eye*, vol. 01, pp. 1–66, 1968.

[15] R. Wildes, J.C. Asmuth and G.L. Green, "A machine Vision System for Iris Recognition," *Machine Vision and Applications*, vol. 9, no. 1, pp. 1432–1769, January 1996.

[16] N. Ritter and R. Owens, "Location of the Pupil-Iris Border in Slit-Lamp Images of the Cornea," *International Conference on Image Analysis and Proceedings*, vol. 00, pp. 740–745, September 27-29, 1999.

[17] Institute of Automation of the Chinese Academy of Sciences, "CASIA V1.0," *CASIA Iris Image Database*, Beijing, China, 2003.

[18] T. M. Montgomery, "Iris image," *Anatomy, Physiology and Pathology of the Human Eye*, 2007. [Online]. Available: http://www.tedmontgomery.com/the_eye/eyephotos/IrisNevus.html

[19] W. Kong and D. Zhang, "Accurate Iris Segmentation based on Novel Reflection and Eyelash Detection Model," *International Symposium on Intelligent Multimedia, Video and Speech Processing*, pp. 263–266, 2001.

[20] W. Boles and B. Boashash, "A Human Identification Technique Using Images of the Iris and Wavelet Transform," *IEEE Transaction on Signal Processing*, vol. 46, no. 4, pp. 1185–1188, April 1998.

[21] P. Burt and E. Adelson, "The Laplacian Pyramid as a Compact Image Code," *IEEE Transactions on Communications*, vol. 31, no. 4, pp. 532–540, 1983.

[22] N. Brady and D. Field, "Local contrast in natural images: normalization and coding efficiency," *Perception*, vol. 29, no. 9, pp. 1041–1055, September 2000.

[23] S. Lim and K. Lee, "Efficient Iris Recognition through Improvement of Feature Vector and Classifier," *Electronics and Telecommunications Research Institute (ETRI Journal)*, vol. 23, no. 2, pp. 61–70, June 2001.

[24] C.L. Tisse, L. Torres and M. Robert, "Person Identification Technique using Human Iris Recognition," *International Conference on Vision Interface, Calgary, Canada*, pp. 294–299, May 27-29, 2002.

[25] Y. Zhu, T. Tan and Y.H. Wang, "Biometric Personal Identification based on Iris Patterns," *15th International Conference on Pattern Recognition*, vol. 2, pp. 801–804, 2000.

[26] J. Daugman, "Recognizing Persons by Their Iris Patterns," *Lecture Notes in Computer Science*, vol. 3338, pp. 5–25, November 2004.

[27] A. Adler and M. Schuckers, "Calculation of a Composite DET Curve," *Lecture Notes in Computer Science*, vol. 3546, pp. 860–868, June 2005.

[28] J. Wayman, "Error Rate Equations for the General Biometric System," *IEEE Transactions on Robotics and Automation Magazine*, vol. 6, pp. 35–48, March 1999.

[29] A. Rukhin and I. Malioutov, "Fusion of Biometric Algorithms in the Recognition Problem," *Pattern Recognition Letters*, vol. 26, no. 5, pp. 679–684, April 2005.

[30] J. Daugman, "Statistical Richness of Visual Phase Information: Update on Recognizing Persons by Iris Patterns," *International Journal of Computer Vision*, vol. 45, no. 1, pp. 25–38, October 2001.

[31] P.J. Phillips, A. Martin, C.L. Wilson, and M. Przybocki, "An Introduction to Evaluating Biometric Systems," *Computer*, vol. 33, no. 2, pp. 56–63, 2000.

[32] A. J. Mansfield and J. L. Wayman, "Best Practices in Testing and Reporting Performance of Biometric Devices," *Centre for Mathematics and Scientific Computing*, National Physical Laboratory (UK) and San Jose State University, August, 2002.

[33] International Biometric Group, "Independent Testing of Iris Recognition Technology ITIRT," *Final Report to the US Department of Homeland Security*, May, 2005.

[34] A. Jain, L. Hong and S. Pankanti, "Biometric Identification," *Communications of the Association for Computing Machinery*, vol. 43, no. 2, pp. 90–98, 2000.

[35] L. Masek and P. Kovesi, "MATLAB Source Code for a Biometric Identification System Based on Iris Patterns," School of Computer Science and Software Engineering, University of Western Australia, Perth, Australia, 2003.

[36] A. Poursaberi1 and B. N. Araabi1, "Iris Recognition for Partially Occluded Images: Methodology and Sensitivity Analysis," *EURASIP Journal on Advances in Signal Processing*, pp. 25–38, March 2006.

[37] G. Deng and L. Cahill, "Multiscale Image Enhancement using the Logarithmic Image Processing Model," *Electronics Letters*, vol. 29, no. 9, pp. 803–804, April 1993.

[38] R. Youmaran, "Automatic Measurement of Features in Ultrasound Images of the Eye," Master's thesis, School of Information and Technology Engineering, University of Ottawa, Ottawa, Canada, 2005.

[39] L. Masek, "Recognition of Human Iris Patterns for Biometric Identification," Master's thesis, School of Computer Science and Software Engineering, University of West Australia, Perth, Australia, 2003.

[40] T. Dembinsky, "Measurement of the Information for Identification in Iris Images," Master's thesis, School of Information and Technology Engineering, University of Ottawa, Ottawa, Canada, 2006.

[41] S. Mika, G. Ratsch, J. Weston, B. Scholkopf and K. Muller, "Fisher Discriminant Analysis with Kernels," *IEEE Neural Networks for Signal Processing Workshop*, pp. 41–48, August 23-25, 1999.

[42] W. Zhao, R. Chellappa and A. Krishnaswamy, "Discriminant Analysis of Principal Components for Face Recognition," *Third International Conference on Automatic Face and Gesture Recognition*, pp. 336–341, April 14-16, 1998.

[43] J. Wayman, A. Jain, D. Maltoni and D. Maio, "An Introduction to Biometric Authentication Systems," *Biometric Systems: Technology, Design and Performance Evaluation*, pp. 1–19, 2004.

[44] T. Manglik and L. Axel, "Use of Bandpass Gabor Filters for Enhancing Blood-Myocardium Contrast and Filling-in tags in tagged MR Images," *International Society for Magnetic Resonance In Medicine*, vol. 3217, no. 11, pp. 2559–2566, May 15-21 2004.

[45] D. Carevic and T. Caelli, "Adaptive Gabor Filters for Texture Segmentation," *The 13th International Conference of Pattern Recognition*, vol. 02, pp. 606–610, August 25-29 1996.

[46] J. Thiem and G. Hartmann, "Biology-Inspired Design of Digital Gabor Filters upon a Hexagonal Sampling Scheme," *The 15th International Conference on Pattern Recognition*, vol. 3, pp. 445–448, September 3-7 2000.

[47] R. Bolle and S. Pankanti, *Biometrics, Personal Identification in Networked Society: Personal Identification in Networked Society.* Kluwer Academic Publishers, Norwell, MA, USA, 1998.